

Article

Crystallographic, Structural, and Electrical Properties of W^{6+} Substituted with Mo^{6+} in Crystalline Phases such as TTB Structure

Hicham Es-soufi ^{1,*} , M. I. Sayyed ^{2,3} , Aljawhara H. Almuqrin ⁴, Raman Rajesh ⁵ , Alan Rogerio Ferreira Lima ⁶, Hssain Bih ⁷  and Lahcen Bih ¹

¹ Laboratory of Sciences and Professions of the Engineer, Materials and Processes Department ENSAM-Meknes Marjane II, Moulay Ismail University, El Mansour, Meknes P.O. Box 15290, Morocco

² Department of Physics, Faculty of Science, Isra University, Amman 11622, Jordan

³ Department of Nuclear Medicine Research, Institute for Research and Medical Consultations (IRMC), Imam Abdulrahman bin Faisal University (IAU), P.O. Box 1982, Dammam 31441, Saudi Arabia

⁴ Department of Physics, College of Science, Princess Nourah bint Abdulrahman University, P.O. Box 84428, Riyadh 11671, Saudi Arabia

⁵ Department of Physics, Velammal College of Engineering & Technology, Madurai 625009, India

⁶ Vasco da Gama CoLAB-Energy Storage, Rua Dr. Roberto Frias, 4200-465 Porto, Portugal

⁷ Process Engineering, Computer Science and Mathematics Laboratory (LIPIM), National School of Applied Engineering-Khouribga, Sultan Moulay Slimane University, Beni Mellal 23000, Morocco

* Correspondence: hichamessoufi@gmail.com

Abstract: Owing to their low dielectric loss and high permittivity values, dielectric ceramics have garnered a lot of interest from the scientific and industrial sectors. These properties allow for their downsizing and use in a variety of electronic circuits. This present work focuses on the impact of the substitution of W^{6+} with Mo^{6+} on the structural and dielectric features of the crystalline phases in a similar TTB structure within the $Ba_{0.54}Na_{0.46}Nb_{1.29}W_{(0.37-x)}Mo_xO_5$ system, with $0 \leq x \leq 0.33$ mol%. These crystalline phases were elaborated using the conventional solid-state reaction method and analyzed with XRD, Raman, and dielectric techniques. The Rietveld refinement method showed that all these phases are characterized by tetragonal structure and the $P4bm$ space group. The Raman spectra corresponded well to a TTB-like structure, and all the bands were assigned. The dielectric measurements of the prepared ceramic samples facilitated the determination of their phase transition temperature (T_c) and the dielectric responses. This investigation focused on determining dielectric permittivity (ϵ') and its correlation with increases in MoO_3 content in the ceramic structure.

Keywords: TTB ceramics; structure; X-ray diffraction; Rietveld method; Raman spectroscopy; dielectric permittivity



Citation: Es-soufi, H.; Sayyed, M.I.; Almuqrin, A.H.; Rajesh, R.; Lima, A.R.F.; Bih, H.; Bih, L.

Crystallographic, Structural, and Electrical Properties of W^{6+} Substituted with Mo^{6+} in Crystalline Phases such as TTB Structure.

Crystals **2023**, *13*, 483. <https://doi.org/10.3390/cryst13030483>

Academic Editor: Jing Guo

Received: 4 February 2023

Revised: 5 March 2023

Accepted: 7 March 2023

Published: 11 March 2023



Copyright: © 2023 by the authors. Licensee MDPI, Basel, Switzerland. This article is an open access article distributed under the terms and conditions of the Creative Commons Attribution (CC BY) license (<https://creativecommons.org/licenses/by/4.0/>).

1. Introduction

Materials of the tetragonal tungsten bronze (TTB) structure type are well-known for their ferroelectric properties [1–5]. Many researchers have investigated these materials for several industrial applications, such as optoelectronics, energy conversions, and chemical sectors [6–10]. This high attention depends on the materials' structural properties. The TTB structure has numerous crystallographic interstices, which enable a broad range of cation replacements. The general chemical formula for the TTB structure is $(A1)_2(A2)_4C_4Nb_{10}O_{30}$, where A1, A2, and C stand for various oxygen sites. The A1 site is surrounded by twelve oxygen ions, while the A2 site is enclosed by eight oxygen ions. The C site is coordinated by six oxygen ions. The cations that can be accommodated by the TTB structure depend on the size of the sites and the charge balance of the structure. Common examples of cations that can be accommodated by the TTB structure include Na^+ , K^+ , Rb^+ , Cs^+ , Ag^+ , Tl^+ , Cu^{2+} , and Pb^{2+} [11–13]. Currently, the advancement of solid solutions has resulted

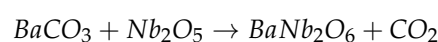
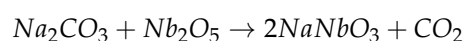
in a multitude of varied distributions of metal cations across different crystallographic locations. This has the potential to enhance physical characteristics, such as dielectric and ferroelectric abilities [14,15]. Several approaches have been developed for enhancing either the structures or properties of ceramics. The usual method to control the electrical characteristics of TTB oxides is nonisovalent replacement based on transition-metal substitution in niobium octahedral sites. This focuses on the property tuning required to produce new phases, including microwave dielectrics [16,17], ionic conductors [18], and ferroelectrics [19–21]. This will eventually lead to the identification of a highly desired, room-temperature multiferroic material. As a result of the variable oxidation state [22], many TTB ferroelectric and ferroelectric-related materials [23–26] exhibit relaxer ferroelectric and dielectric phenomena [27–30]. TTB structures are classically derived from well-known perovskite-type structures and characterized by high electrical performance [31,32]. Compounds similar to tetragonal tungsten bronze oxides, along with perovskites, comprise one of the most significant groups of ferroelectrics. Many works have reported the existence of phases containing different transition metals related to the tetragonal tungsten bronze structure [33]. There have been initiatives to use Ta, Mo, or Nb in place of W [33]. For instance, Ikeda et al. [34] investigated the results of replacing Nb ions with W ions in the niobates of the TTB structure. Similarly, a detailed investigation of “Ferroelectric and Related Substances on $\text{Ba}_3\text{Na}_3\text{MoNb}_9\text{O}_{30}$ ” has also been reported [35]. According to Marinder [36], an X-ray diffraction analysis of the $\text{NaNbO}_3\text{-Nb}_2\text{O}_5\text{-WO}_3$ system illustrated that a few phases are associated with the TTB structure. High-resolution electron microscopy analysis of the aforementioned system revealed many structural types that are linked to the TTB structure [37]. Further, the $\text{NaNbO}_3\text{-WO}_3$ system’s mixed oxides are a subject of attention among the numerous current TTB structures. When a low-temperature method is used, the composition with a 1:1 ratio of the end members of this system appears effective for producing NaNbWO_6 , exhibiting a phase that resembles the TTB structure. However, this shows that a complex X-ray pattern has been considered as a combination of different phases [38–41]. Alternatively, the ceramic method was claimed to be able to prepare a single phase of NaNbWO_6 that is similar to TTB [42], but an electron diffraction examination showed that this composition comprises two closely related tetragonal and monoclinic phases [43].

The primary focus of the present exploration is to examine the influence of Mo^{6+} content on the structural and dielectric characteristics of tetragonal tungsten bronze (TTB) within the $\text{NaNbO}_3\text{-WO}_3\text{-BaNb}_2\text{O}_6$ system. For this purpose, the incorporation effect of molybdenum into tungsten sites on the structural and electrical properties of $\text{Ba}_{0.54}\text{Na}_{0.46}\text{Nb}_{1.29}\text{W}_{(0.37-x)}\text{Mo}_x\text{O}_5$ ($0 \leq x \leq 0.33$) ceramics is investigated.

2. Experimental Section

2.1. Ceramic Sample Synthesis

The conventional solid-state technique was applied to synthesize the crystalline phases of the $\text{Ba}_{0.54}\text{Na}_{0.46}\text{Nb}_{1.29}\text{W}_{(0.37-x)}\text{Mo}_x\text{O}_5$ system ($x = 0.04, 0.08, \text{ and } 0.33$), as described in the experimental protocol for our previous work [44]. This experimental protocol for preparation of the crystalline phases within the $\text{NaNbO}_3\text{-BaNb}_2\text{O}_6\text{-WO}_3/\text{MoO}_3$ system involves two steps. The first one is focused on preparation of the crystalline phases NaNbO_3 and BaNb_2O_6 from the raw materials BaCO_3 , Na_2CO_3 , and Nb_2O_5 (purchased from Merck (Merck, 99.95%)) according to the following reactions:



These raw materials were mixed and ground in agate mortar around one hour later, according to their stoichiometry coefficient, and then subjected to thermal treatment at 1100°C for 24 h. The second stage involved mixing and grinding for two hours: the obtained oxides, NaNbO_3 and BaNb_2O_6 , were processed in stoichiometric proportions

with the oxides WO_3 and/or MoO_3 (bought from Merck, 99.95%) for about an hour. The mixture was then put into an alumina crucible and heated to $1200\text{ }^\circ\text{C}$ for 12 h, then reapplied while ethanol was used for about one hour so that it could be calcined. In an alumina crucible, calcination was carried out for 24 h upon reaching a temperature of $1300\text{ }^\circ\text{C}$ for the final heating. The grinding and calcination processes were carried out two more times. XRD analysis was utilized to investigate the formation of the compound.

2.2. Characterization Techniques

The prepared ceramics were examined at ambient temperatures using a Bruker D8 Advance diffractometer utilizing $CuK\alpha$ ($\alpha = 1.540598\text{ \AA}$). The X-ray diffractograms were recorded from 10° to 100° , with a step size of 0.01° . GSAS-II software [45] was utilized to apply the Rietveld refinement to validate and quantify the crystalline phases found in the composite ceramics, followed by sinterization. The phases that were present in the composites under study were identified using the Crystallography Open Database (COD) [46]. The ceramics were subjected to Raman analysis at room temperature, utilizing a spectrometer with a HORIBA-Jobin laser light that was directed onto each sample through a microscope lens. To conduct dielectric analysis, the disk-shaped samples were initially smoothed down, and to ensure optimal electrical contact, silver paste was applied on both sides of each specimen. The capacitance (C_p) and loss factor ($\tan\delta$) were analyzed over a frequency range of 20 Hz to 1 MHz. An impedance analyzer was used to apply a 0.5 V source to the electrode pellets. Measurements were conducted between $25\text{ }^\circ\text{C}$ and $550\text{ }^\circ\text{C}$ using a Linkam TS 93 hot stage that offered a temperature stability of $\pm 0.1\text{ K}$. To create the capacitor-shaped pieces, platinum electrodes were positioned on two of the ceramic's round faces. The real part (ϵ') and loss ($\tan\delta$) of the dielectric permittivity, as well as the ac conductivity (σ_{ac}), were determined using Equations (1)–(3) [32,47]:

$$\epsilon' = \frac{C_p t}{\epsilon_0 A} \quad (1)$$

$$\sigma_{ac} = \omega \epsilon_0 \epsilon'' \quad (2)$$

$$\tan \delta = \frac{\epsilon''}{\epsilon'} \quad (3)$$

In these equations, t , A , ω , ϵ_0 , and ϵ'' (equal to ϵ' multiplied by the tangent of δ) represent the layer of the disk-shaped piece, the cross-sectional area of the electrode, the angular frequency, the permittivity of free space, and the imaginary component of the complex dielectric constant, respectively.

3. Results and Discussion

3.1. X-ray Diffractograms

Figure 1a displays the XRD diffractograms of all the examined samples. The XRD pattern of the sample ($x = 0$) significantly changed as the concentration of Mo^{6+} increased, as shown in Figure 1b. All examined sample ceramics had very significant diffraction peaks, which suggested that these compounds were well-crystallized. Additionally, all XRD patterns of the prepared ceramics exhibited a tetragonal-type structure. However, it seems that except for ($x = 0$), the patterns contained a secondary phase: scheelite-type $BaMoO_4$ (barium molybdate). The peak of the index (004) was the characteristic secondary phase located at 2θ position 26.42, which was identified according to JPD5 NO: 029-0193. This peak appeared from the ceramic composite where $x = 0.04$, and it was characterized by low intensity (see Figure 1b). Figure 1c–e display the X-ray diffractograms of the samples obtained from the Rietveld refinement process. The constituent features of the composites where $x = 0.04$, $x = 0.08$, and $x = 0.33$ were guaranteed by the Rietveld refinement; however, the composite where $x = 0.33$ was guaranteed to have the properties of both the $Ba_{0.54}Na_{0.46}Nb_{1.29}W_{0.04}Mo_{0.33}O_5$ and purity ($BaMoO_4$) constituents. Each plot displays the parameters derived with the Rietveld refinement. For all compositions, the

goodness of fit (GOF), or χ^2 , parameters were below three, which points to the improved XRD patterns' high dependability (see Table 1). Furthermore, Rietveld refinement confirmed the tetragonal structure of a similar TTB phase with the P4bm space group and a minor BaMoO₄ impurity peak (marked with \blacklozenge) (see Figure 1b). As opposed to this, the ferroelectric phase and the P4bm space group created a similar TTB structure. G. Yanalak et al have already provided in-depth descriptions of the BaMoO₄ phase [48]. A structure of this type is consistently favored, as it promotes better interaction between the ferroelectric and BaMoO₄ phases, consequently leading to a robust microwave dielectric effect in composites [49]. Improvement in the volume of the composites was readily observed as the lattice parameters, a, b, and c, were somewhat raised with rising MoO₃ content in the ferroelectric phase. The substitution of W⁶⁺ (0.74 Å) with Mo⁶⁺ (0.73 Å) [50] led to the formation of the BaMoO₄ phase (tetragonal with the I41/a space group). In comparison of the x = 0.00 composite to other composites, the cell parameters and volume increased as the peak intensity of the BaMoO₄ composite increased from x = 0.00 to x = 0.33. This variation may be associated with the increase in the content of the BaMoO₄ phase in the composites. To ensure the secondary phase would be dependent on the BaMoO₄ phase type, the dielectric properties of the current pieces were studied to see how their dielectric permittivity would change with increased BaMoO₄ composite (see the dielectric measurements section).

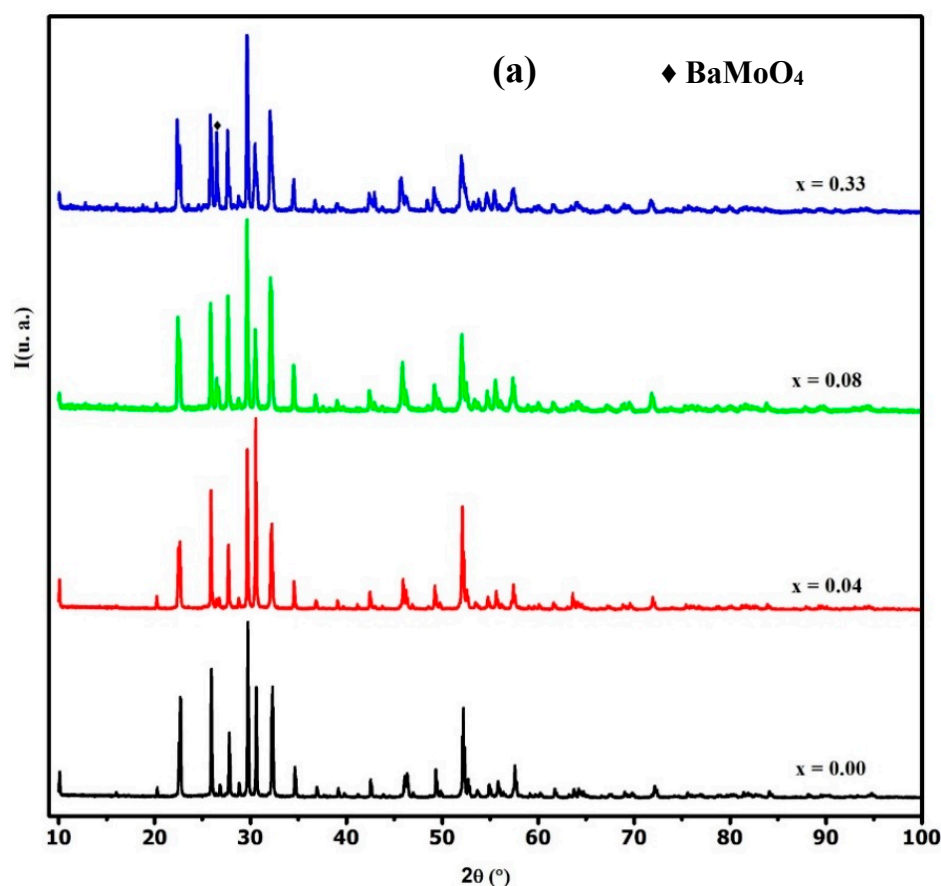


Figure 1. Cont.

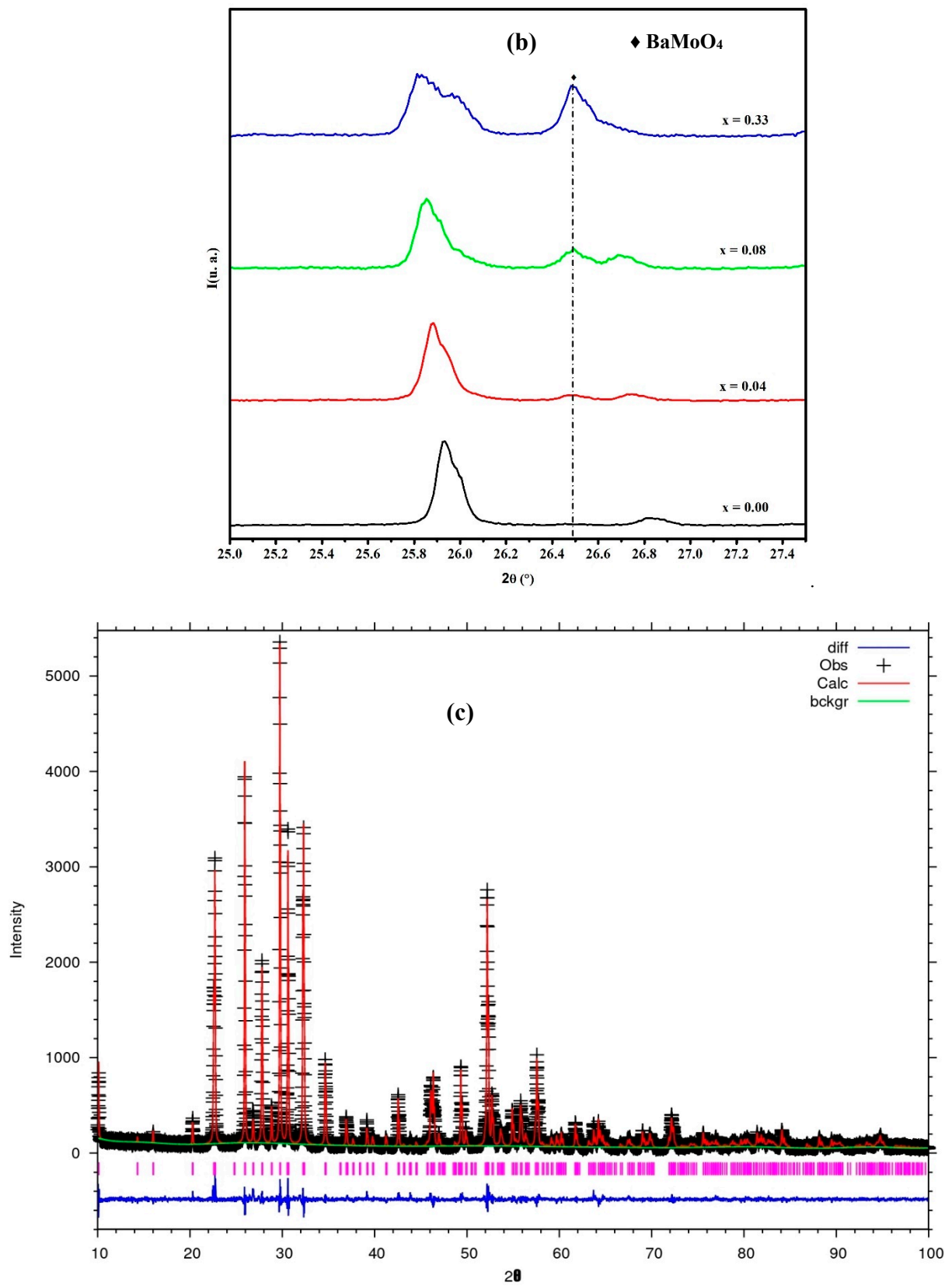


Figure 1. Cont.

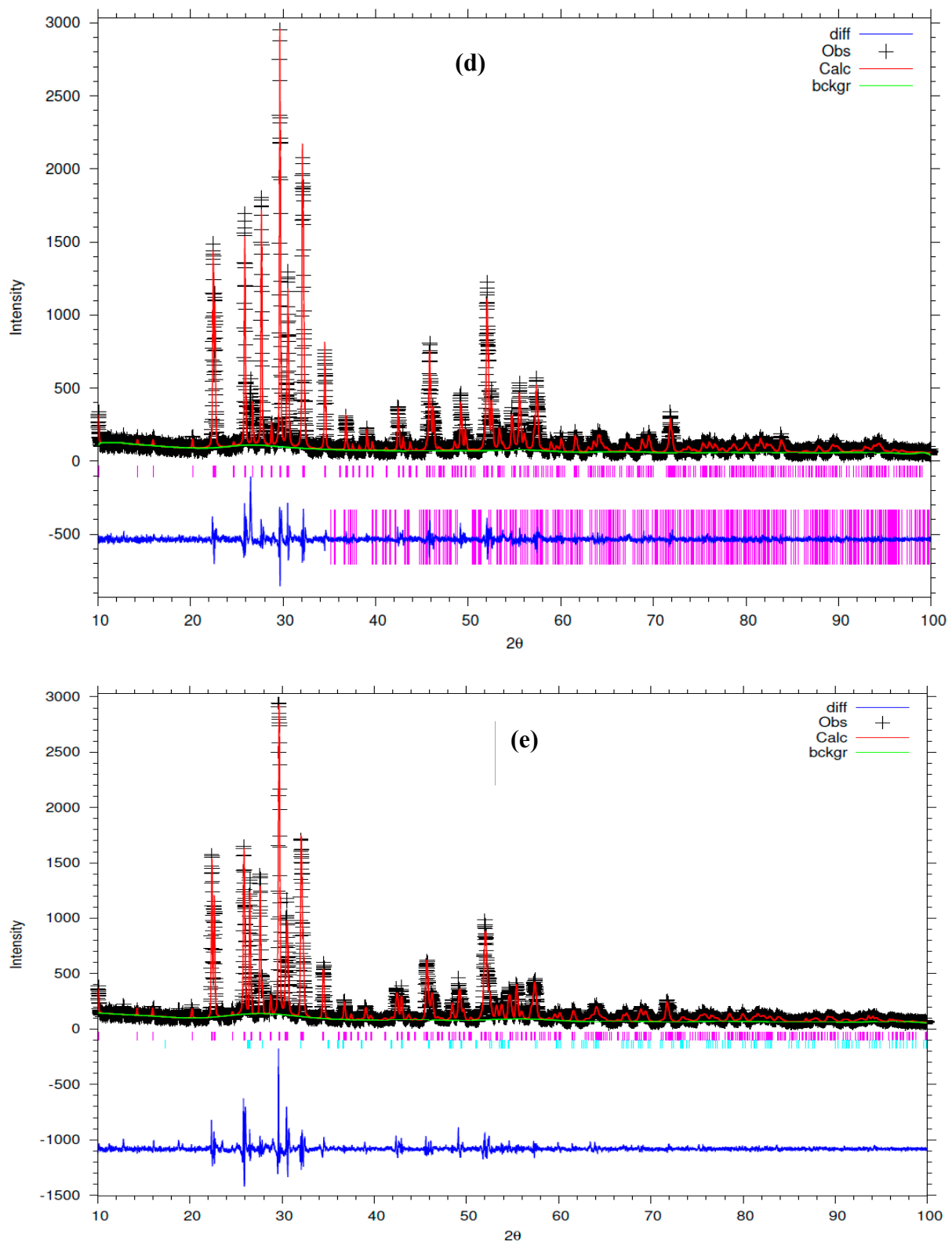


Figure 1. Combined X-ray diffraction patterns (a,b) and Rietveld refinement of Ba_{0.54}Na_{0.46}Nb_{1.29}W_(0.37-x)Mo_xO₅ ceramics (x = 0.04 (c), x = 0.08 (d), and x = 0.33 (e)).

Table 1. The data from the Rietveld refinement for the crystalline phases of the $\text{Ba}_{0.54}\text{Na}_{0.46}\text{Nb}_{1.29}\text{W}_{(0.37-x)}\text{Mo}_x\text{O}_5$ system ($x = 0.04, 0.08, \text{ and } 0.33$).

Composition	$x = 0.04$	$x = 0.08$	$x = 0.33$
Symmetry	Tetragonal	Tetragonal	Phase 1: Tetragonal; Phase 2: Tetragonal
Space Group	P4bm	P4bm	Phase 1: P4bm Phase 2: I 41/a
Z	6	6	Phase 1: 6 Phase 2: 4
Lattice Parameters (Å)	$a = b = 12.40430$ (10); $c = 3.95059$ (6)	$a = b = 12.41525$ (12); $c = 3.95844$ (7)	Phase 1: $a = b = 12.41681$ (17); $c = 3.97203$ (8) Phase 2: $a = b = 5.59091$ (22); $c = 12.8173$ (7)
Volume (Å ³)	607.865 (15)	610.146 (15)	Phase 1: 612.396 (21) Phase 2: 400.65 (4)
Calculated Density (g/cm ³)	5.729	5.698	Phase 1: 5.272 Phase 2: 4.928
Chemical Formula Weight (g/mol)	349.52	348.96	Phase 1: 324.02 Phase 2: 297.27
R_p	7.79	9.51	10.11
R_{wp}	10.48	12.69	13.26
χ^2	1.837	2.249	2.744
GOF	1.36	1.50	1.66

The Rietveld refinement of the XRD patterns corresponding to the prepared ceramics of $\text{Ba}_{0.54}\text{Na}_{0.46}\text{Nb}_{1.29}\text{W}_{(0.37-x)}\text{Mo}_x\text{O}_5$ ($x = 0.04, 0.08, \text{ and } 0.33$) was fitted with a tetragonal (P4bm) model developed from the model of the previous crystalline phase [44]. Starting where $x = 0.04$, the Ba^{2+} and Na^+ cations occupied two sites in this developed model. Here, Na_1^+ was placed in the Wyckoff position of Ba_1^{2+} at the 2a (0, 0, z) sites, and Na_2^+ was placed in Ba_2^{2+} at the 4c (x, y, z) sites, respectively. However, the Nb^{5+} , W^{6+} , and Mo^{6+} occupied two different sites in the Wyckoff position. That is, the Nb_1^{5+} , W_1^{6+} , and Mo_1^{6+} were placed in the 2b (0, 0.5, 0.5) sites, whereas the Nb_2^{5+} , along with the W_2^{6+} , occupied the 8d (x, y, z) sites. Further, the O^{2-} oxygen dianions occupied the 8d (x, y, z), 4c (x, y, z), and 2b (0, 0.5, z) Wyckoff sites. While comparing the $x = 0.04$ composition with the $x = 0.08$ composition, we found a difference in that where $x = 0.08$, which manifested as Nb_1^{6+} with Mo_1^{6+} occupying the 2b (0, 0.5, 0.5) sites and Nb_2^{6+} with Mo_2^{6+} occupying the 8d (x, y, z) sites (see Table 2). However, in the composition ($x = 0.33$) model, Nb_1^{5+} and Mo_1^{6+} occupied the 2b (0, 0.5, 0.5) sites, and Nb_2^{5+} and Mo_2^{6+} with W_2^{6+} occupied the 8d (x, y, z) sites (see Table 2). Furthermore, the atomic positions of the secondary phase, BaMoO_4 ($a = b = 5.5909$ Å and $c = 12.8173$ Å), were determined. In this structure ($x = 0.33$), the Ba^{2+} and Mo^{6+} cations occupied, respectively, the 4b (0, y, z) and the 4a (0, y, z) sites, and the oxygen dianions occupied the 16f (x, y, z) Wyckoff sites. In Table 3, we list the interatomic distances. The crystallographic parameters of the refined compositions ($x = 0.04, 0.08, \text{ and } 0.33$) revealed that oxygen atoms surrounded sodium and barium atoms, creating deformed and irregular surroundings. The average distance between the sodium (1) and barium (1) atoms and the oxygen atoms was approximately 2.71 Å ($x = 0.00$)–2.88 Å ($x = 0.33$) [44]. Figure 2 illustrates the [1 1 1] projection of the crystal structure where $x = 0.33$. The Na^+ and Ba^{2+} cations were found to occupy sites with coordination numbers of 15 and 12, respectively. The octahedral sites were occupied by two cations of Nb^{5+} , W^{6+} , and/or Mo^{6+} . In addition, the crystal structure exhibited a P4bm space group, allowing for small, off-center displacements of Nb, W, and Mo within the (Nb/W/Mo) O_6 octahedra. The Ba (1)/Na (1) atoms were encompassed by 12 O⁻ atoms, with the faces of the Nb1/W1/Mo1@O6 octahedra being shared. The polyhedron distances ranged from 1.93 Å ($x = 0.00$) to 1.98 Å ($x = 0.33$), with an estimated value of less than $d(\text{Ba}(1)/\text{Na}(1)@O) = 2.71$ Å ($x = 0.00$)–2.88 Å ($x = 0.33$). It is worth noting that an average of

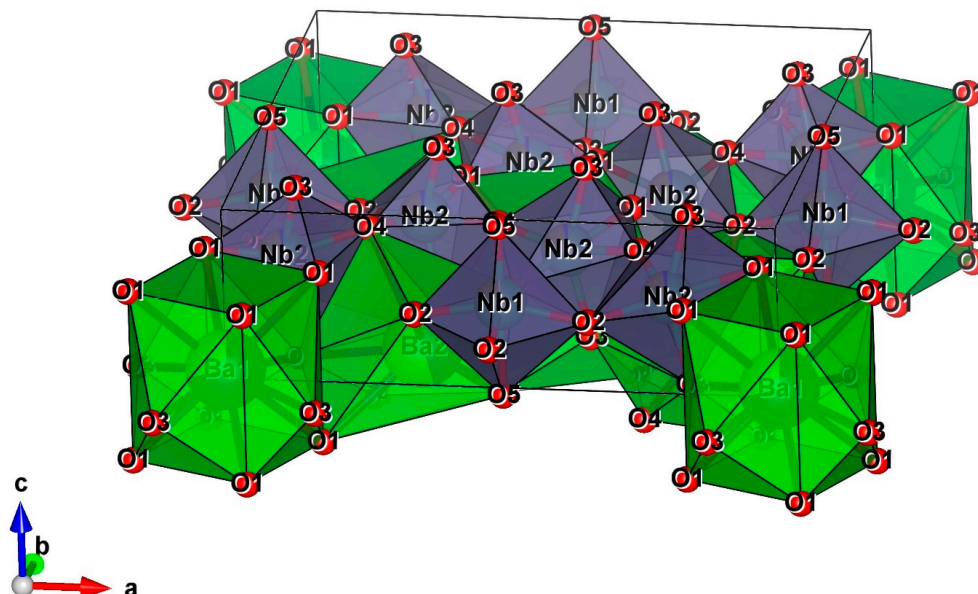
15 oxygen atoms enclosed the barium (2) and sodium (2) atoms, with the distance varying from 3.02 Å (0.00) to 2.74 Å ($x = 33$). Nonetheless, there was a slight distinction in the atomic positions of the Ba (2) and Na (2) atoms, as shown in Table 2 [44]. The Nb(1), Mo(1), or W(1) atoms were surrounded by six oxygen atoms, forming octahedrons that were linked together at their tips. The average distance between the atoms ranged from 2.04 Å ($x = 0.00$) to 2.05 Å ($x = 0.00$).

Table 2. Atomic positions of the $\text{Ba}_{0.54}\text{Na}_{0.46}\text{Nb}_{1.29}\text{W}_{(0.37-x)}\text{Mo}_x\text{O}_5$ system ($x = 0.04, 0.08, \text{ and } 0.33$).

Composition	Atom	Wyckoff	x	y	z	Occupation	U_{iso}	
X = 0.04	Ba1	2a	0	0	0.05	0.716	0.800 (12)	
	Na1	2a	0	0	0.05	0.284	0.800 (12)	
	Ba2	4c	0.17310 (15)	0.67310 (15)	0.01270 (15)	0.454	0.0524 (9)	
	Na2	4c	0.17310 (15)	0.67310 (15)	0.01270 (15)	0.546	0.0524 (9)	
	Nb1	2b	0	0.5	0.5	0.82	0.0301 (9)	
	W1	2b	0	0.5	0.5	0.039	0.09	
	Mo1	2b	0	0.5	0.5	0.125	0.03077	
	Nb2	8d	0.07581 (8)	0.20922 (8)	0.50822 (8)	0.761	0.2105 (19)	
	W2	8d	0.07581 (8)	0.20922 (8)	0.50822 (8)	0.239	0.00555	
	O1	8d	0.1337 (9)	0.0825 (8)	0.446 (10)	1	0.1174 (30)	
	O2	8d	0.3543 (8)	0.0126 (10)	0.402 (9)	1	0.1174 (30)	
	O3	8d	0.0473 (10)	0.1997 (8)	0.065 (7)	1	0.1174 (30)	
	O4	4c	0.294	0.794	0.575	1	0.1174 (30)	
	O5	2b	0	0.5	−0.02	1	0.65 (6)	
	X = 0.08	Ba1	2a	0	0	0.05	0.716	0.800 (11)
Na1		2a	0	0	0.05	0.284	0.800 (11)	
Ba2		4c	0.17347 (13)	0.67347 (13)	0.01308 (13)	0.454	0.0204 (7)	
Na2		4c	0.17347 (13)	0.67347 (13)	0.01308 (13)	0.546	0.0069 (7)	
Nb1		2b	0	0.5	0.5	0.75	0.0332 (8)	
Mo1		2b	0	0.5	0.5	0.25	0.0329 (8)	
Nb2		8d	0.07595 (9)	0.20935 (9)	0.50835 (9)	0.761	0.01819 (34)	
W2		8d	0.07595 (9)	0.20935 (9)	0.50835 (9)	0.239	0.79798 (34)	
O1		8d	0.1567 (9)	0.0724 (10)	0.535 (12)	1	0.1116 (16)	
O2		8d	0.3447 (6)	0.0140 (6)	0.519 (12)	1	0.0092 (16)	
O3		8d	0.0560 (7)	0.2038 (6)	0.032 (7)	1	0.0287 (16)	
O4		4c	0.2844 (7)	0.7844 (7)	0.581 (5)	1	0.0190 (16)	
O5		2b	0	0.5	−0.02	1	0.0532 (16)	
X = 0.33		Ba1	2a	0	0	0.05	0.716	0.800 (13)
		Na1	2a	0	0	0.05	0.284	0.800 (13)
	Ba2	4c	0.17500 (19)	0.67500 (19)	0.01460 (19)	0.454	0.0239 (10)	
	Na2	4c	0.17500 (19)	0.67500 (19)	0.01460 (19)	0.546	0.0239 (10)	
	Nb1	2b	0	0.5	0.5	0.82	0.0328 (12)	
	Mo1	2b	0	0.5	0.5	0.164	0.0328 (12)	
	Nb2	8d	0.07176 (13)	0.21142 (14)	0.4854 (16)	0.761	0.0324 (4)	
	Mo2	8d	0.07176 (13)	0.21142 (14)	0.4854 (16)	0.20775	0.0324 (4)	
	W2	8d	0.07176 (13)	0.21142 (14)	0.4854 (16)	0.03125	0.0324 (4)	
	O1	8d	0.1609 (8)	0.0615 (8)	0.568 (4)	1	0.0294 (21)	
	O2	8d	0.3426 (8)	0.0055 (8)	0.411 (5)	1	0.0294 (21)	
	O3	8d	0.1022 (8)	0.1772 (8)	−0.069 (5)	1	0.0294 (21)	
	O4	4c	0.2860 (8)	0.7860 (8)	0.582 (5)	1	0.0078 (21)	
	O5	2b	0	0.5	−0.045 (12)	1	0.0078 (21)	
	BaMoO ₄	Ba	4b	0	0.25	0.625	1	−0.0085 (11)
Mo		4a	0	0.25	0.125	1	0.0402 (27)	
O		16f	0.175 (8)	0.203 (12)	0.0231 (26)	1	0.08796	

Table 3. Different interatomic distances (Å) of the crystalline phases of $\text{Ba}_{0.54}\text{Na}_{0.46}\text{Nb}_{1.29}\text{W}_{(0.37-x)}\text{Mo}_x\text{O}_5$ ($x = 0.04, 0.08, \text{ and } 0.33$).

Composition	0.04	0.08	0.33
Principal Interatomic Distances (Å)			
Ba1/Na1–O			
Ba1/Na1–O1	3.080×4	2.8773×4	2.8705×4
Ba1/Na1–O1	2.501×4	2.9578×4	2.9678×4
Ba1/Na1–O3	2.546×4	2.650×4	2.5836×4
(Ba1/Na1–O)	2.709	2.8283	2.88073
Principal Interatomic Distances (Å)			
Ba2/Na2–O			
Ba2/Na2–O1	3.465×2	-	-
Ba2/Na2–O1	3.153×2	-	-
Ba2/Na2–O2	3.145×2	2.826×2	2.6375×2
Ba2/Na2–O2	2.539×2	-	-
Ba2/Na2–O4	2.7364×2	2.593×2	2.5984×2
Ba2/Na2–O4	3.0713×2		2.9797
(Ba2/Na2–O)	3.0182	2.7095	2.7385
Principal Interatomic Distances (Å)			
Nb1/W1/Mo1–O			
Nb1/W1/Mo1–O2	1.855×4	1.9374×4	1.9873×4
Nb1/W1/Mo1–O5	2.05431	1.9001	1.8073
Nb1/W1/Mo1–O5	1.89629	2.0584	2.1648
(Nb1/W1/Mo1–O)	1.93519	1.9353	1.9864
Principal Interatomic Distances (Å)			
Nb2/W2/Mo2–O			
Nb2/W2/Mo2–O1	1.745	1.9572	2.1904
Nb2/W2/Mo2–O1	2.190	1.9766	-
Nb2/W2/Mo2–O2	2.340	-	1.9133
Nb2/W2/Mo2–O3	1.791	1.9030	1.8591
Nb2/W2/Mo2–O3	2.230	2.0887	2.2743
Nb2/W2/Mo2–O4	1.9451	-	2.0308
Nb2/W2/Mo2–O	2.0402	1.9813	2.0535

**Figure 2.** Crystal structure where $x = 0.33$, projected in 3D space ([1 1 1]).

3.2. Characterization with Raman Spectroscopy

The crystallographic study of the crystalline phases of $\text{Ba}_{0.54}\text{Na}_{0.46}\text{Nb}_{1.29}\text{W}_{(0.37-x)}\text{Mo}_x\text{O}_5$ ($x = 0.04, 0.08, \text{ and } 0.33$) showed that the structures of these ceramics are formed from different bonds, such as Ba/Na-O, Nb/W/Mo-O, and Ba/Na-Nb/W/Mo. The vibration modes of these principal bonds were able to be identified with Raman spectroscopy. As shown in Figure 3, the Raman spectra were recorded between 1200 and 100 cm^{-1} of these prepared ceramics, characterized by different bands. The identification of these bonds with their bands has been made (see the Table 4) in reference to our previous work focused on crystalline phases ($x = 0.0$) [44].

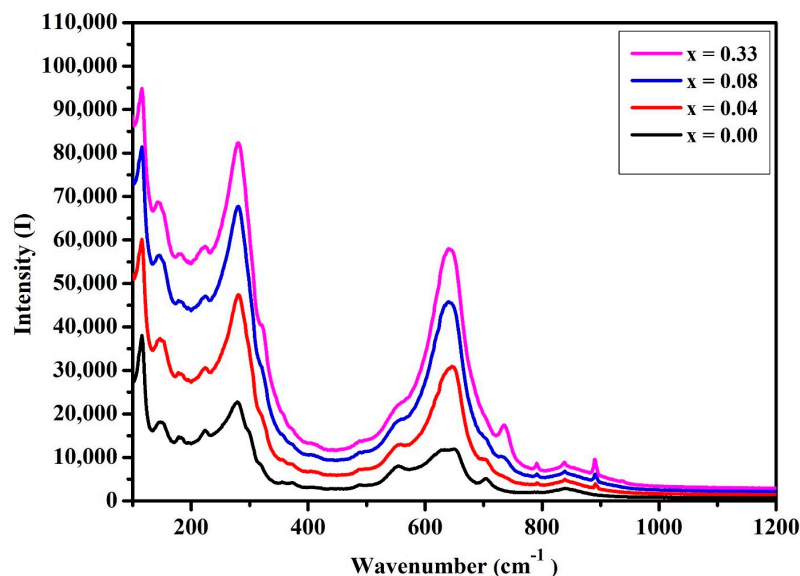


Figure 3. Raman spectra of the $\text{Ba}_{0.54}\text{Na}_{0.46}\text{Nb}_{1.29}\text{W}_{(0.37-x)}\text{Mo}_x\text{O}_5$ ($x = 0, 0.04, 0.08, 0.33$) ceramics.

Table 4. The Raman bands in the range of $1200\text{--}100\text{ cm}^{-1}$ were identified for the $\text{Ba}_{0.54}\text{Na}_{0.46}\text{Nb}_{1.29}\text{W}_{(0.37-x)}\text{Mo}_x\text{O}_5$ ceramics.

Band Position (cm^{-1})	Assignment
485→115	Octahedra (Mo/W/NbO_6) or cation translation vibrations ($\text{Ba}^{2+}, \text{Na}^+$)
650→485	Mo/W/Nb-O stretching vibrations caused by deformation
840→650	Mo/W/Nb-O bonds

Stretching vibrations of Mo/W/Nb-O bonds were the primary Raman bands within the $840\text{--}650\text{ cm}^{-1}$ region, while the deformation modes of Mo/W/Nb-O bonds were found in the bands between 650 cm^{-1} and 485 cm^{-1} . The bands in the range of $485\text{--}115\text{ cm}^{-1}$ may have been linked with W/Mo/Nb-O bonds in the octahedra (W/Mo/NbO_6) or vibrations of cation translation ($\text{Ba}^{2+}, \text{Na}^+$). Additionally, according to Shudong Xu et al. [50], the band at 250 cm^{-1} is attributed to O-Nb-O bending vibrations. The bands located between 280 and 650 cm^{-1} are related to NbO_6 -octahedron bending and stretching vibrations. This is similar to the modes observed in LiNbO_3 at 248 cm^{-1} and 628 cm^{-1} and in $\text{Pb}_{2(1-x)}\text{K}_{1+x}\text{Gd}_x\text{Nb}_5\text{O}_{15}$ at $260\text{--}280\text{ cm}^{-1}$ and $630\text{--}650\text{ cm}^{-1}$ [51]. In addition, there is a possibility that the highest-frequency mode, in the range of $850\text{--}938\text{ cm}^{-1}$, could be associated with the stretching vibration of $(\text{Nb/W/Mo})\text{O}_6$ octahedra, similarly to perovskites [52]. The Raman spectrum of $\text{Ba}_{0.54}\text{Na}_{0.46}\text{Nb}_{1.29}\text{W}_{0.37}\text{O}_5$ displayed a broad and strong peak at approximately 650 cm^{-1} , as well as another intense peak around 280 cm^{-1} . These peaks are attributed to Nb-O vibrations in the NbO_6 octahedra (Figure 3) [44]. Furthermore, from the composition where $x = 0.04$ with the substitution of W^{6+} (0.74) with Mo^{6+} (0.73), the intensity of the Raman peaks at the 280 cm^{-1} and 650 cm^{-1} positions increased with increasing MoO_3

content. These two Raman peaks are associated with the Nb/W/MoO₆ octahedra, and the increasing of their peak intensities can be explained via an increased number of MoO₆ octahedra. Furthermore, increasing the MoO₆ content in the framework had no effect on the Raman peak positions because the W⁶⁺ and Mo⁶⁺ ions were the same size and occupied the same sites (Wyckoff 2 and 8). On the other side, few Raman peaks of low intensities were observed from the composition where $x = 0.04$, and their intensities began to increase as MoO₃ content increased; these Raman peaks may be characteristic of the formation of the scheelite-type BaMoO₄ composite. Thus, the Raman analysis validated the Rietveld refinement of the X-ray data obtained using the proposed refinement models and verified the presence of a secondary phase (BaMoO₄).

3.3. Dielectric Analysis

3.3.1. Evolution of Dielectric Permittivity (ϵ^*) with Temperature

Figure 4a–d depict the thermal evolution of the dielectric permittivity (ϵ') during heating of different solid-solution compositions ($x = 0.00, 0.04, 0.08, \text{ and } 0.33$) at different frequencies.

The ferroelectric character of the Ba_{0.54}Na_{0.46}Nb_{1.29}W_(0.37-x)Mo_xO₅ solid solution at room temperature was confirmed for all compositions. Thus, we were able to highlight the characteristic anomaly of a phase transition, ferroelectric–paraelectric, at the transition temperature, T_c . The position of the peak was independent of the frequency; hence, the behavior of the ferroelectric studied was of a classical character. As a result, we observed a decrease in the ceramic's dielectric permittivity of an increase in the rate of substitution (x) (see Figure 1e). It should also be noted that at high frequencies, the anomaly completely vanished and the ceramic lost its properties; this behavior was brought on by a reduction in contribution of polarization mechanisms. As is well known, conductivity contributes to loss of storage energy, as seen with the drop in the maximum of ϵ' at the level of the transition. Ionic conduction or space charges are related to this evolution. Consequently, degradation of dielectric characteristics can be used to explain this phenomenon (related to the increase in conductivity, which presents a disadvantage for ferroelectrics) [53]. The ferroelectric characteristics of the ceramics under study, such as those where $x = 0.00, x = 0.04, x = 0.08, \text{ and } x = 0.33$, are grouped in Table 5. It should be observed that the effect of the substitution showed up as a reduction in the real permittivity's maximum ϵ'_{max} value, which would typically fall as “ x ” rose (see Table 5). Depending on the substitution, this drop can be explained by a loss of stored energy in the ceramic samples [53] or can be demonstrated with the formation of phase-type BaMoO₄, characterized by low dielectric permittivity, as F.A.C. Nobrega et al. [49] confirmed.

Table 5. The ferroelectric properties of the Ba_{0.54}Na_{0.46}Nb_{1.29}W_(0.37-x)Mo_xO₅ solid solution where $0 \leq x \leq 0.33$.

Composition	T_c	ϵ'_{max} 1 KHz	ϵ'_{max} 10 KHz	ϵ'_{max} 100 KHz	ϵ'_{max} 1000 KHz
0.00	250.84	1770.90	668.33	408.37	328.97
0.04	276.57	844.84	342.88	242.48	222.40
0.08	288.36	399.49	235.21	191.40	174.97
0.33	285.48	369.48	189.51	161.58	155.37

3.3.2. Evolution of Dielectric Losses ($\tan\delta$) with Temperature

The dielectric losses, $\tan(\delta) = \frac{\epsilon''}{\epsilon'}$, in the ferroelectric phase were reasonably low for all of the compositions examined, as shown in Figure 5a–d. We saw that the losses significantly rose during the paraelectric phase. At low frequencies and high temperatures, this rise was larger. This demonstrates that conductivity plays a vital role at high temperatures [54].

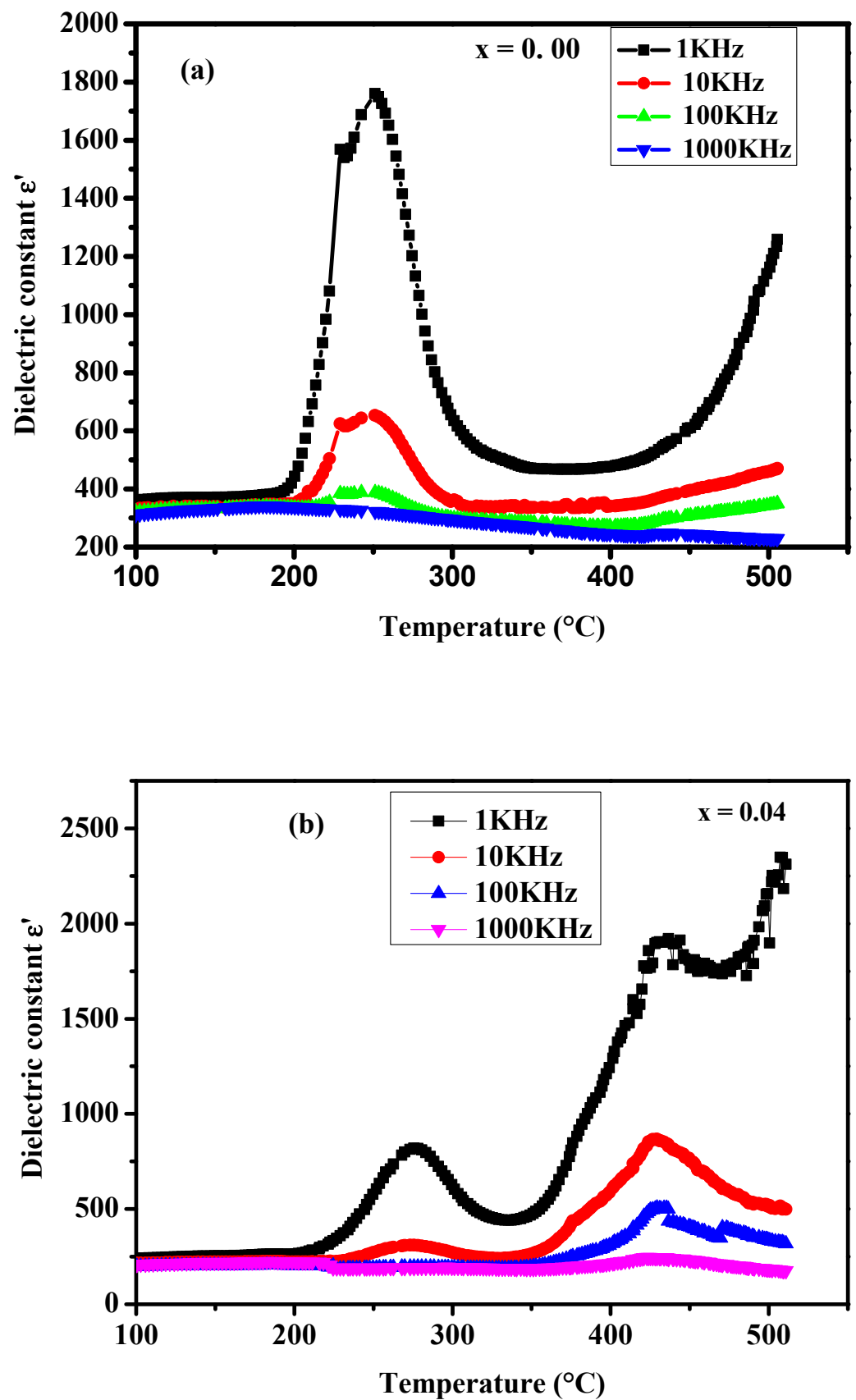


Figure 4. Cont.

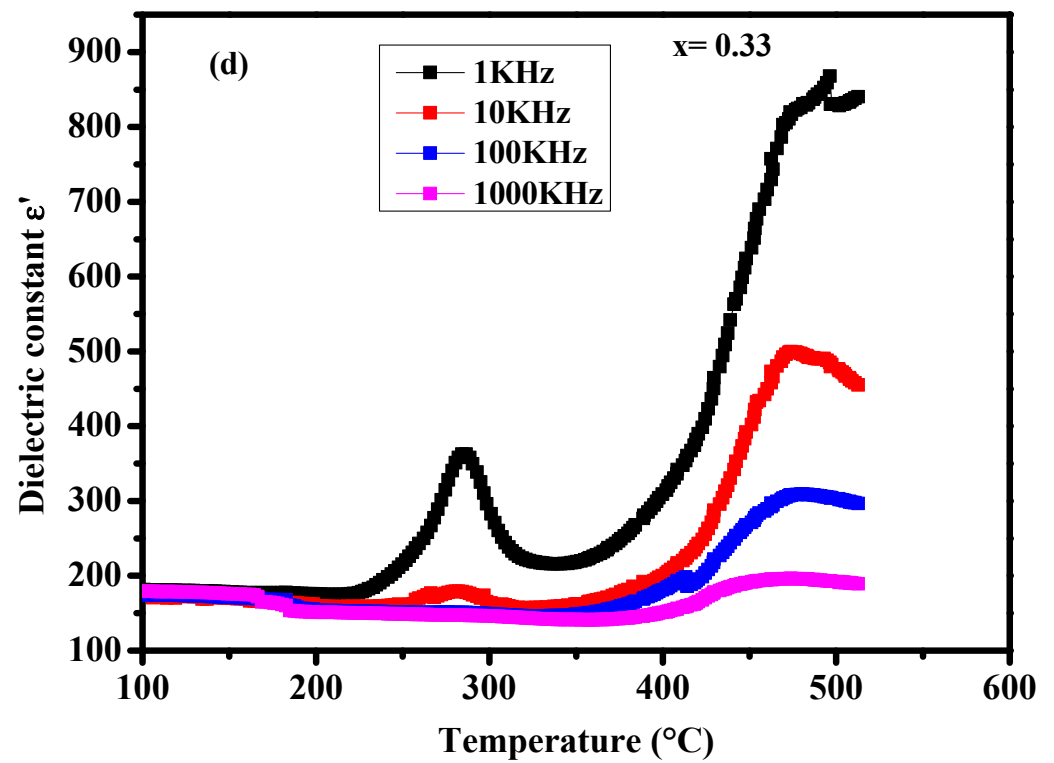
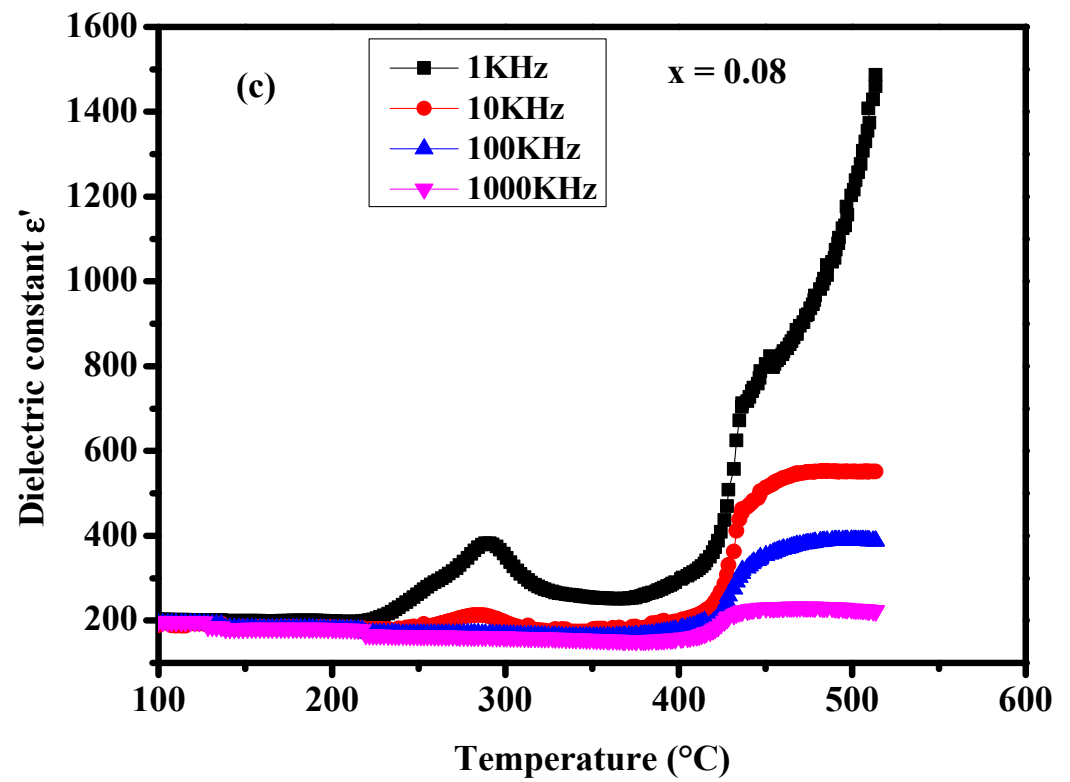


Figure 4. Cont.

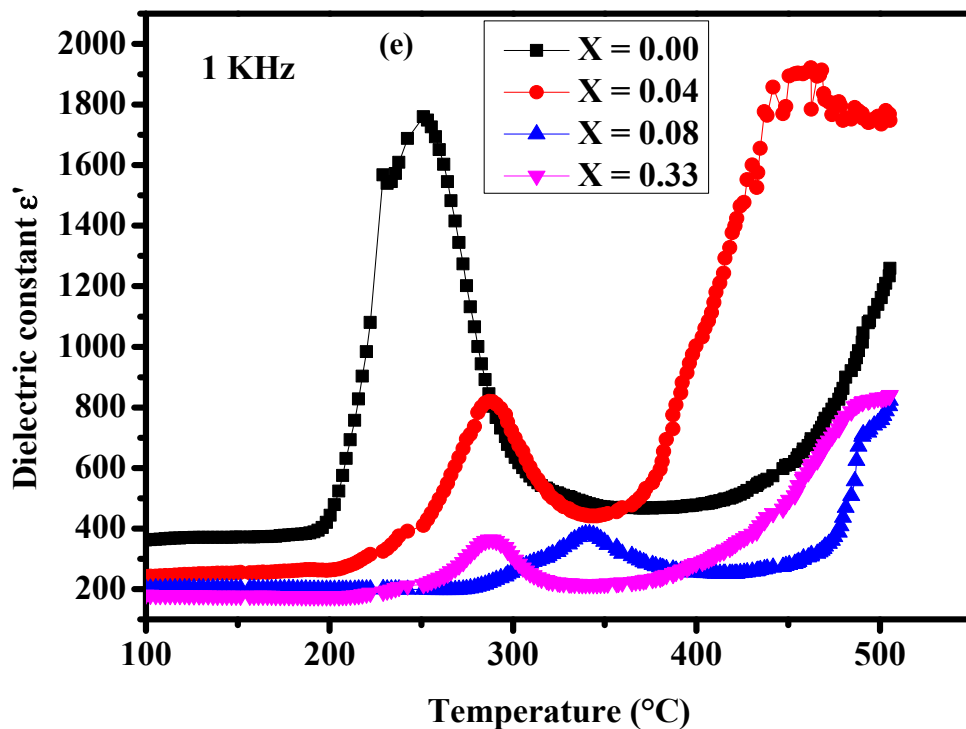


Figure 4. (a–e) Thermal evolution of ϵ_r' at different frequencies and at different compositions for $x = 0.00, 0.04, 0.08$ and 0.33 .

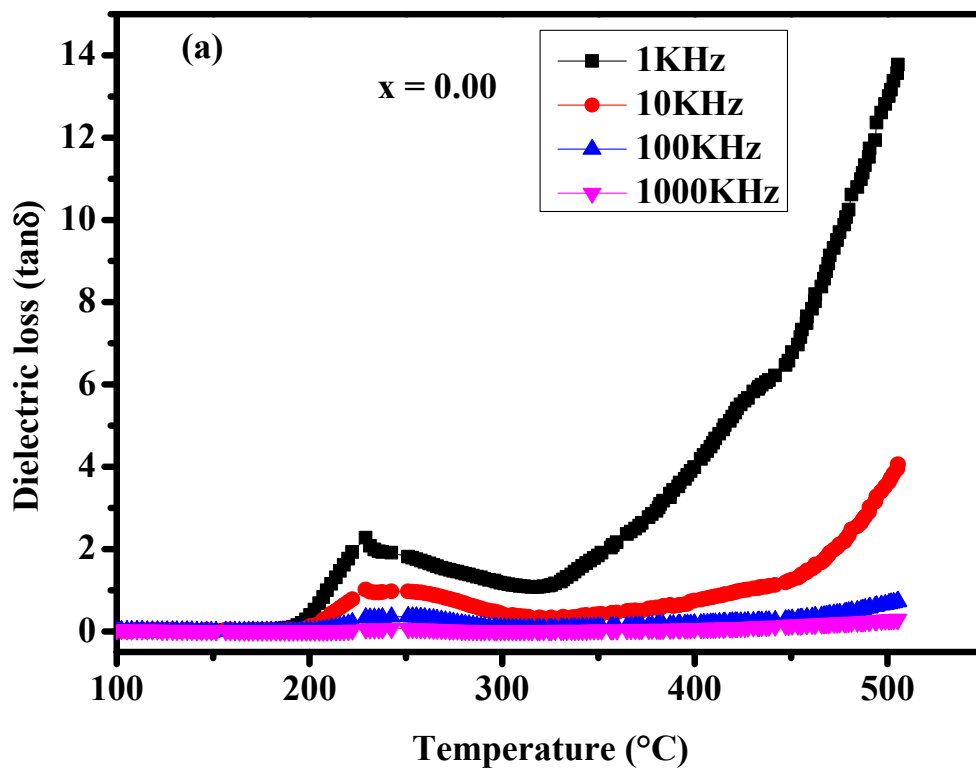


Figure 5. Cont.

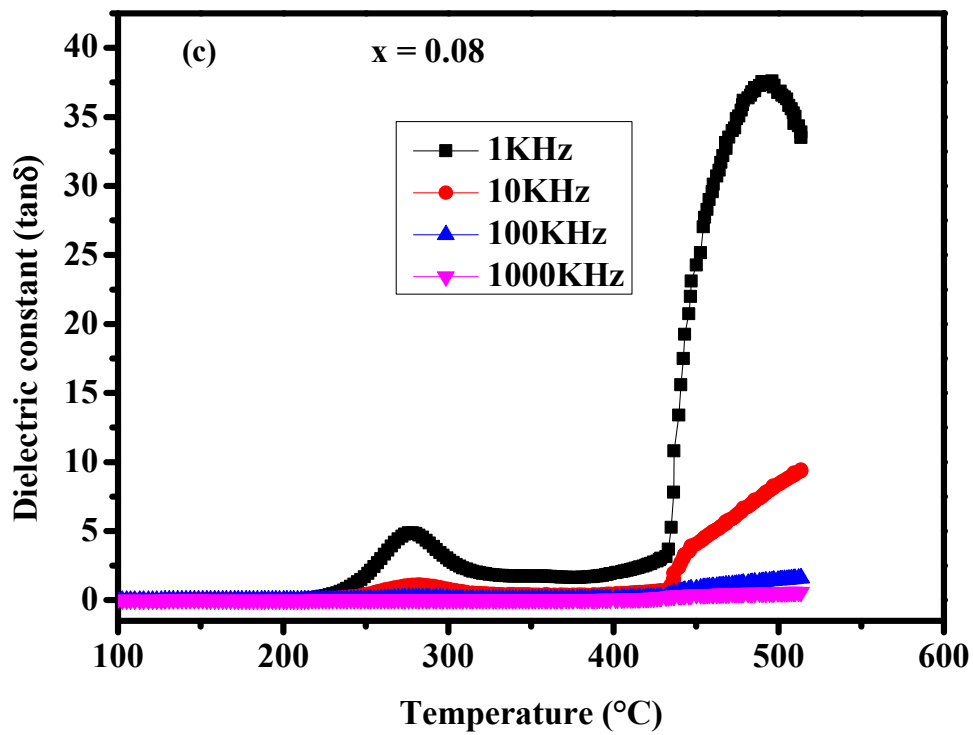
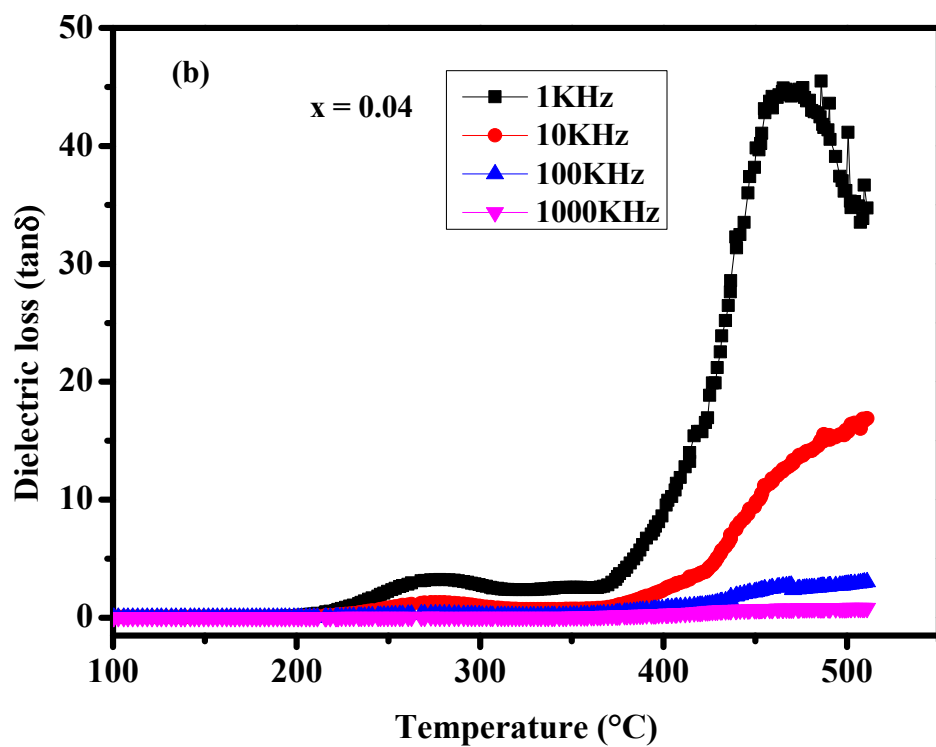


Figure 5. Cont.

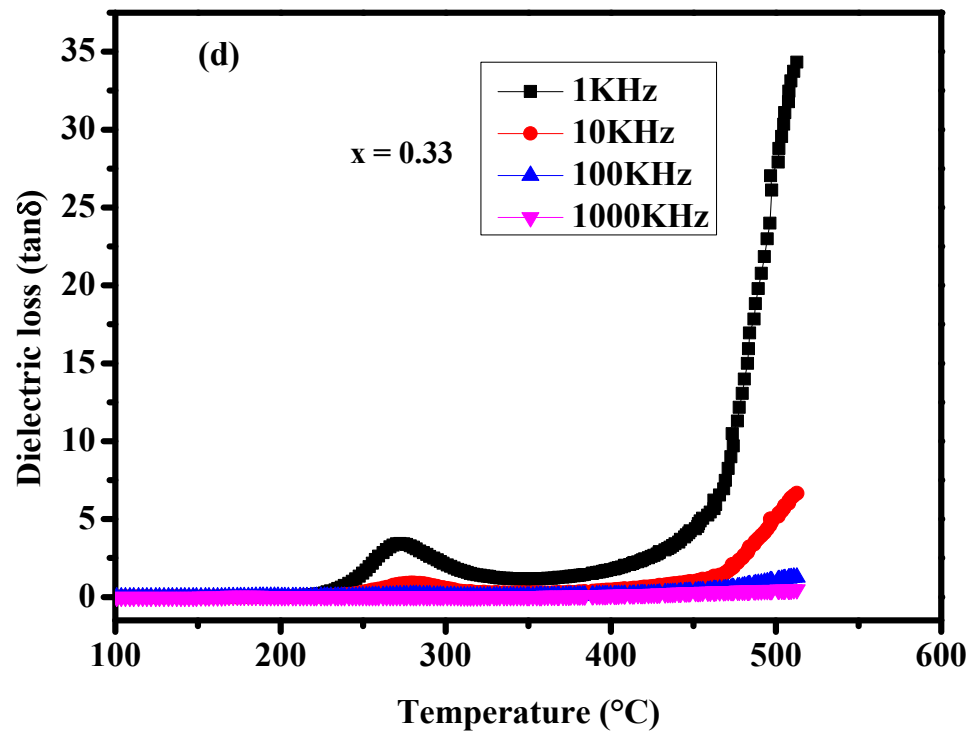


Figure 5. (a–d) Evolution in dielectric loss with respect to temperature is plotted for the prepared ceramics.

3.3.3. Phase Transition Order

This study focused on analyzing changes in inverse dielectric permittivity with temperature to understand the characteristics of phase transitions. Figure 6a–d depict the variation of the opposite dielectric permittivity versus temperature during heating at a frequency of 1 kHz. The shape of the curve for all of the compositions followed the Curie–Weiss law well in the paraelectric phase defined by Equation (4) [55]:

$$\varepsilon' = \frac{C}{T - T_0} \quad (4)$$

The experimental data fitted were used to calculate the Curie constants and the Curie–Weiss temperatures for various compounds (see Figure 6a–d). The comparison of the calculated temperatures, T_0 , and those deduced from the curves of variation of the real part and the value of the Curie–Weiss constant allowed us to determine the transition order and type.

The Curie–Weiss law was clearly observed in the ceramic samples, and the paraelectric phase exhibited a linear dependence that described the law. Table 6 lists the results in groups. The transition was of the first order, since T_c and T_0 were not coincident. The Curie constant, C , was of the order of 10^3 K in the case of an order–disorder-type transition; however, displacive transitions take values 100 times higher, as demonstrated in the literature [56]. Because the Curie constant values for the different ceramics ranged from 10^4 to 10^5 K, the transition was displacive in nature.

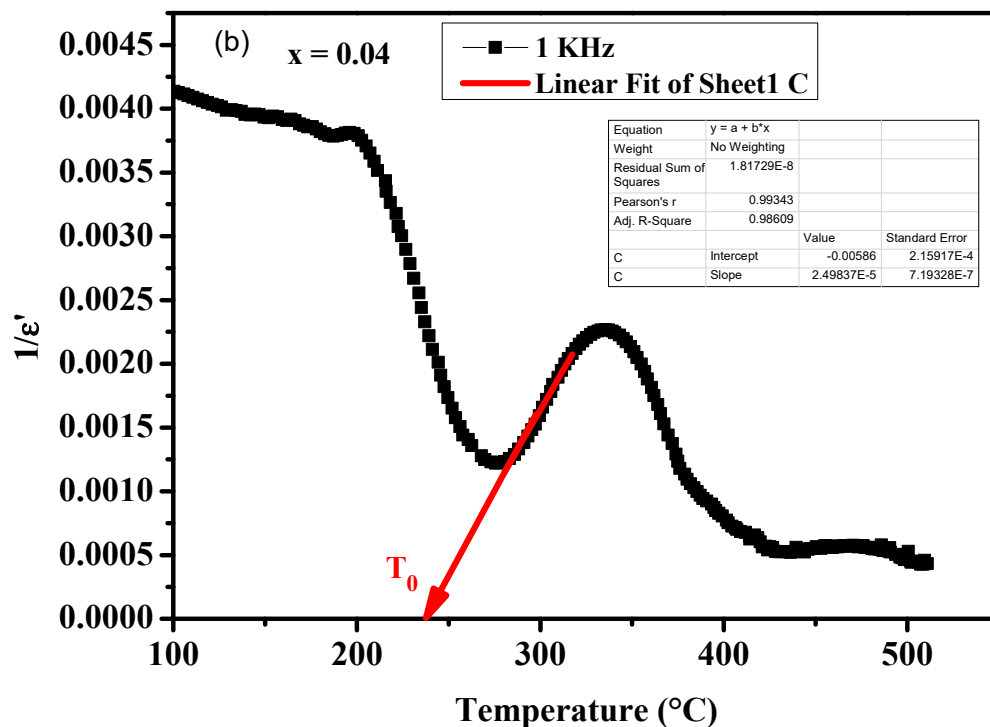
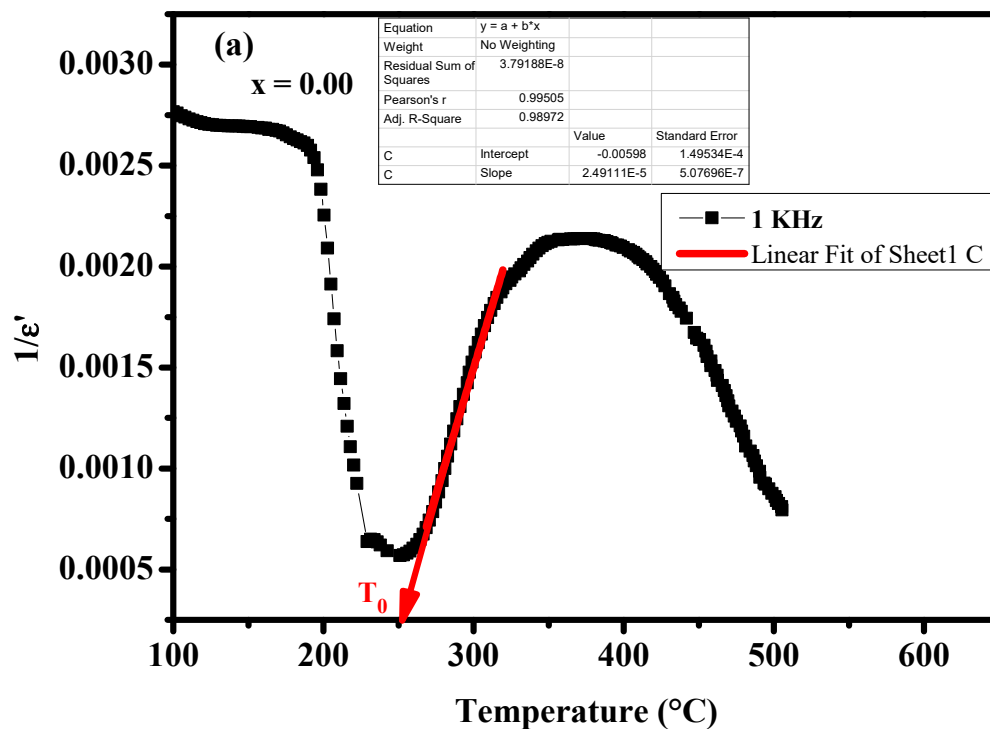


Figure 6. Cont.

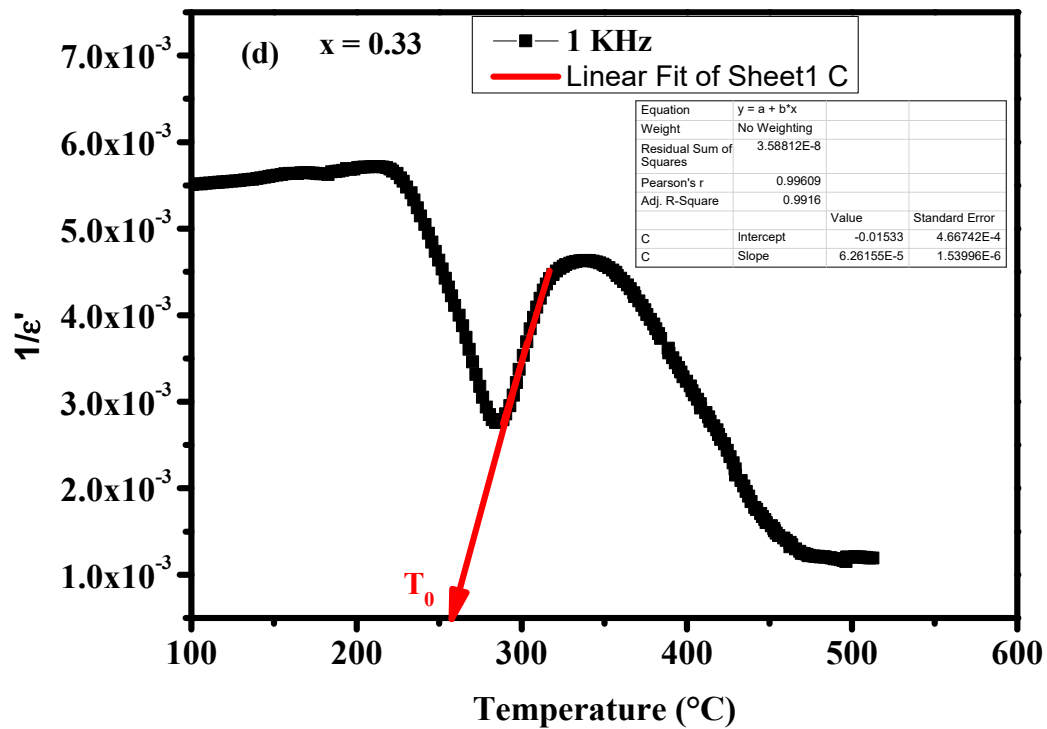
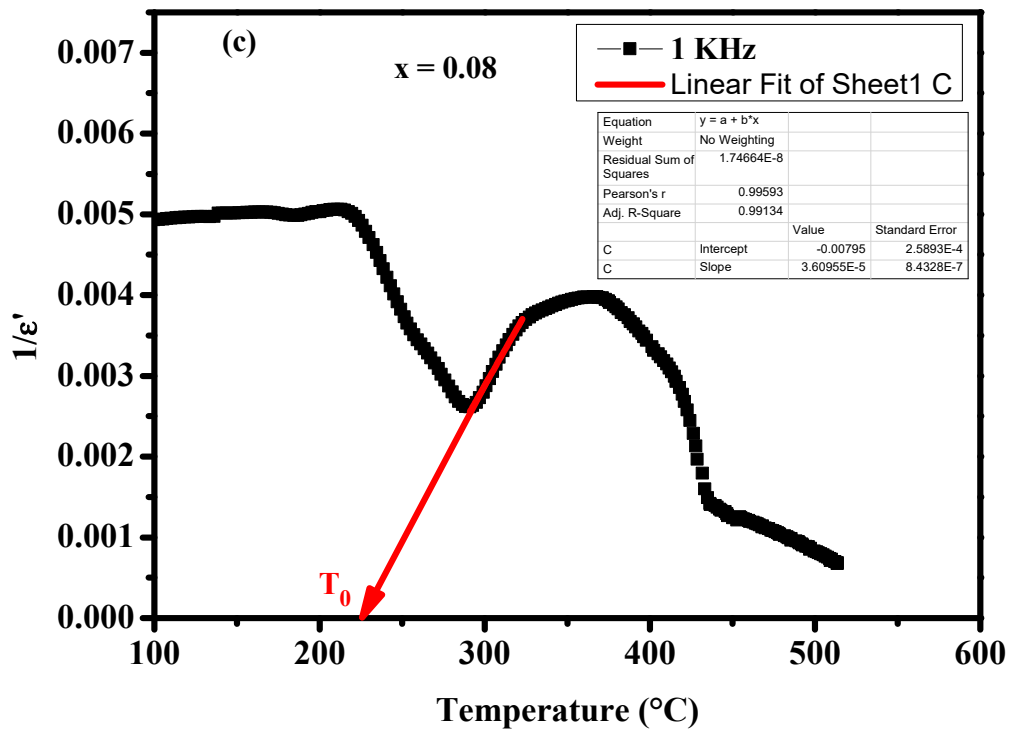


Figure 6. (a–d) Thermal evolution of $\frac{1}{\epsilon_r'}$ at a 1 KHz frequency for the ceramics.

Table 6. Curie–Weiss parameters for the investigated solid solution.

Composition	T_c	T_0	C
x = 0.00	250.84	253.18	40.16×10^3
x = 0.04	276.57	237.68	40.00×10^3
x = 0.08	288.36	225.70	27.70×10^3
x = 0.33	285.48	257.57	15.92×10^3

Additionally, from Table 6, it is noted that the temperature, T_c , passed through a high where $x = 0.08$ ($T_c = 288.36$) and then decreased where $x = 0.33$ ($T_c = 285.48$), highlighting the impact of the replacement on the ferroelectric characteristics. J. Ravez [56] stated that although the size of alkaline earth cations and the size of alkaline cations do not appear to be directly related to the Curie temperature (T_c), an increase in distortion occurs. The single lone pair of electrons in $5s^2$, which caused an increase in the distortion of the octahedra, and the strongly polarized nonspherical cations in Ba^{2+} were both responsible for the composition's high T_c value ($x = 0.08$) [57]. As a result, the structural distortion and the contribution of the W^{6+} cations to spontaneous polarization were increased; thus, the substitution of Mo^{6+} in W^{6+} increased the T_c range for the ceramics of the compositions where $x \leq 0.08$ [58]. Further, the Mo–O bond's deterioration also supported this increasing trend. However, a slight decrease in the Curie temperature was observed in the compositions where $x > 0.08$; this behavior is explained by the fact that the pace at which the Mo^{6+} cations occupied the octahedral sites surpassed that of the W^{6+} cations. Additionally, ferroelectricity is more likely to arise when a metal cation is smaller. Other experimental research on TTB-structured ferroelectric materials, with $Ba_{2(1-x)}Pb_{2.05x}Na_{1-0.1x}Nb_5O_{15}$ and $Pb_{2(1-x)}Gd_xK_{1+x}Nb_5O_{15}$, has been conducted [59–62]. In it, this process was explained by changes in the polarization axis, which can also occur in the solution investigated in this work, as well as reorientation of dipoles [55].

3.3.4. Study of the Conductivity in the Solid Solution

Furthermore, there was a significant increase in the loss coefficients for high temperatures, phase paraelectrics, and low frequencies, indicating the presence of conductivity in the ceramics [63]. These anomalies in the dielectric loss curves near the transition temperature were also noted during the study of the thermal variation of the real part of the dielectric permittivity. Consequently, we can see that the loss decreased as the frequency increased, as shown in Figure 7a–d.

Ionic conduction, which is caused by movement of charge carriers, can account for this increase in conductivity at high temperatures and low frequencies [64]. The charge carriers' inability to adhere to excitation of the electric field at high frequencies accounts for conductivity's diminishing tendency at these frequencies [65].

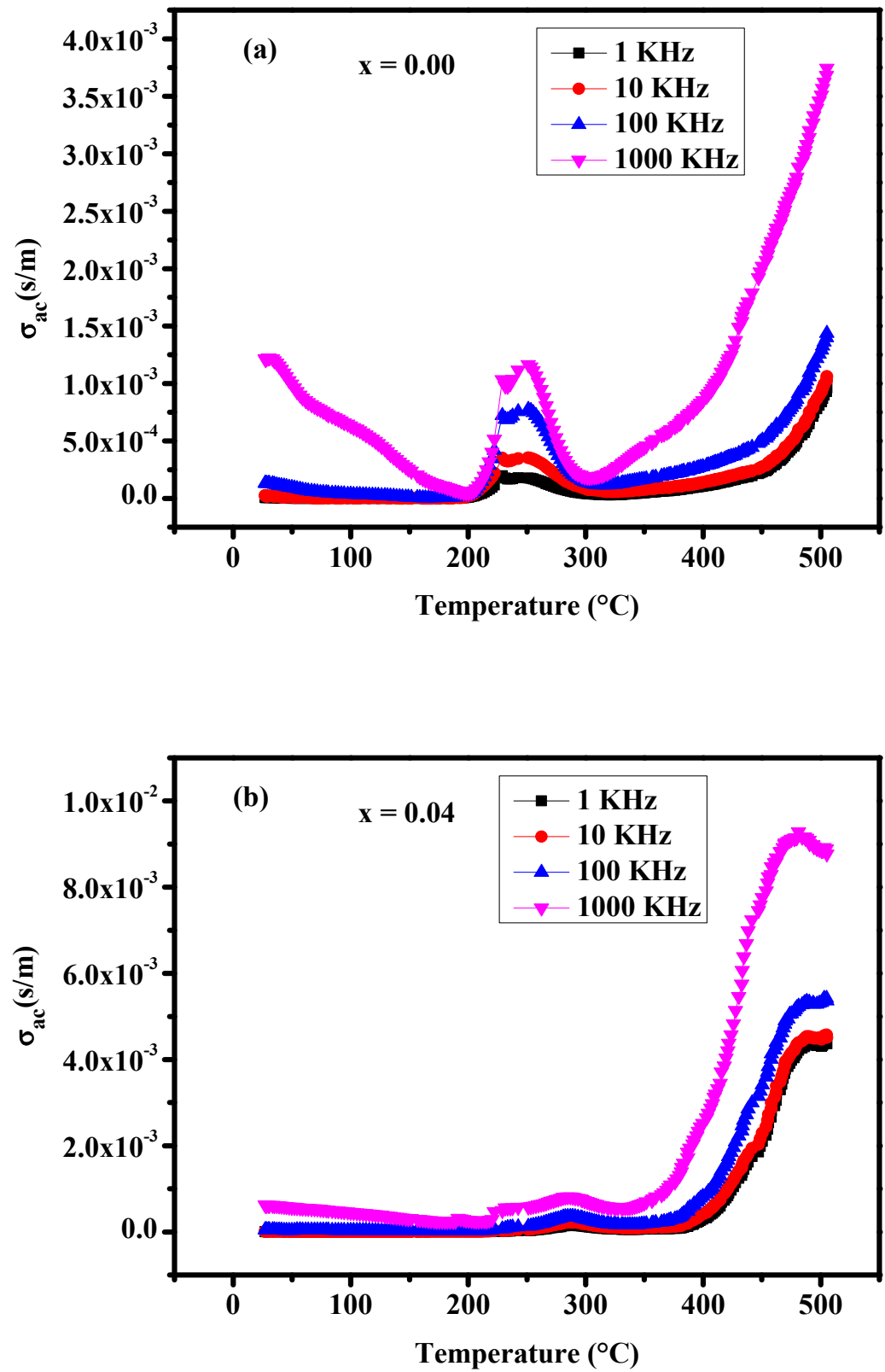


Figure 7. Cont.

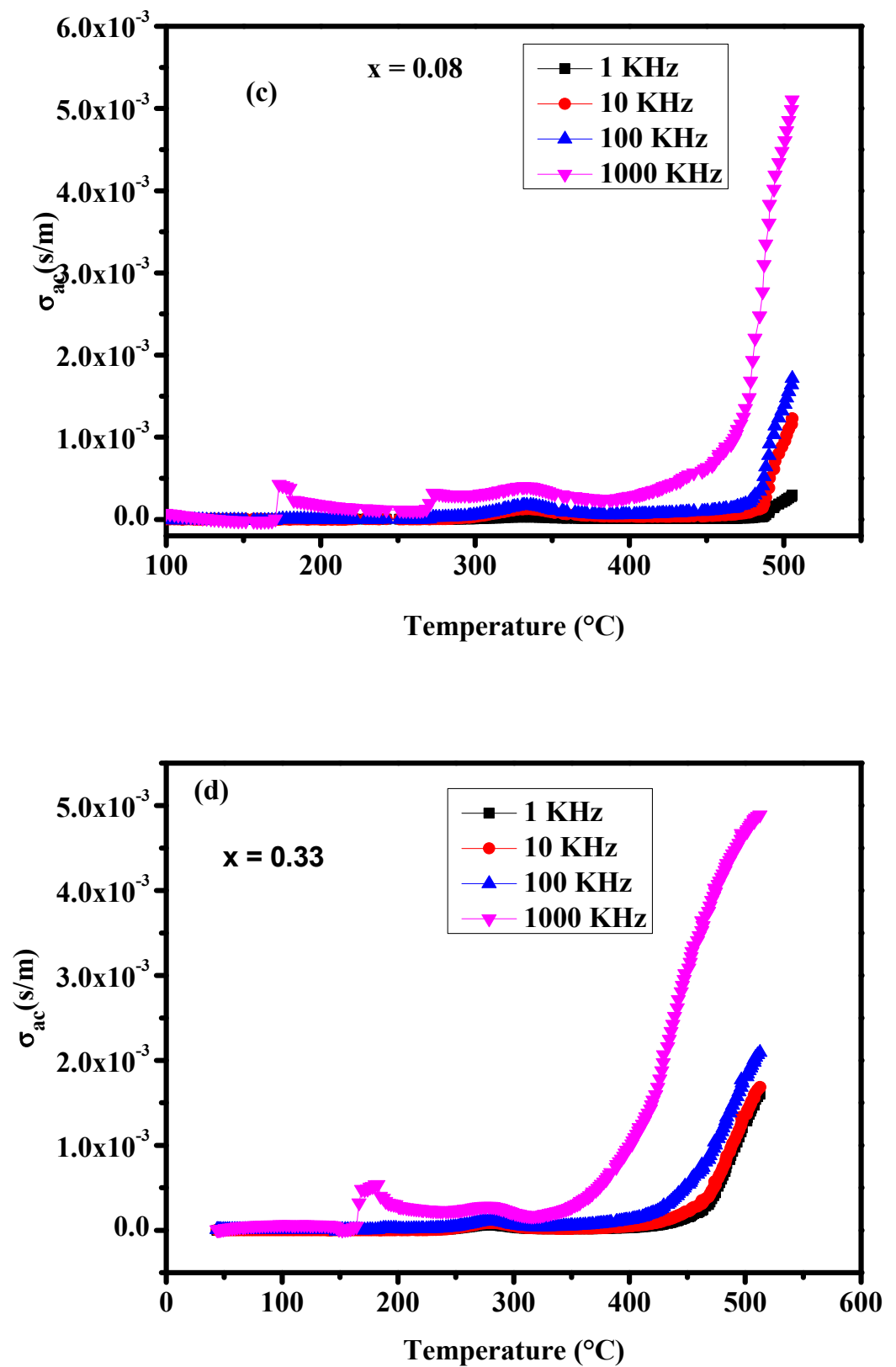


Figure 7. (a–d) Thermal development of electrical conductivity at different frequencies for the ceramics.

4. Conclusions

The crystalline phases of the $\text{Ba}_{0.54}\text{Na}_{0.46}\text{Nb}_{1.29}\text{W}_{(0.37-x)}\text{Mo}_x\text{O}_5$ system were synthesized through a solid-state route. The Rietveld method was used to simulate the XRD data of various $\text{Ba}_{0.54}\text{Na}_{0.46}\text{Nb}_{1.29}\text{W}_{(0.37-x)}\text{Mo}_x\text{O}_5$ samples, confirming that these samples crystallize in a tetragonal structure with the P4bm space group, in addition to the presence of a small amount of the BaMoO_4 phase type (tetragonal with the I41/a space group). Raman investigation results confirmed that substitution of W^{6+} (0.74 Å) with Mo^{6+} (0.73 Å) prompts the formation of the secondary phase, BaMoO_4 . The dielectric measurements of these ceramics across a wide range of temperatures (from 25 °C to 550 °C) and frequencies (from 20 Hz to 1 MHz) led to the observation of a transition from the ferroelectric phase to the first-order paraelectric phase. This investigation demonstrated a decrease in ϵ'_{max} due to the substitution of W^{6+} with Mo^{6+} at a certain frequency. This dielectric study also allowed us to analyze under study the evolution of the system according to the substitution. The Curie–Weiss law's parameters brought to light the examined system's behavior, which shifted from a displacive-type transition to an order–disorder-type transition. The charge carriers' inability to adhere to the excitation of the electric field at high frequencies accounted for the conductivity's diminishing tendency at these frequencies.

Author Contributions: Conceptualization, H.E.-s.; methodology, H.E.-s.; software, H.E.-s., A.R.F.L. and R.R.; formal analysis, H.E.-s.; investigation, H.B.; data curation, H.E.-s.; writing—original draft preparation, H.E.-s.; writing—review and editing, H.E.-s. and R.R.; visualization, H.B.; supervision, L.B.; project administration, M.I.S.; funding acquisition, A.H.A. All authors have read and agreed to the published version of the manuscript.

Funding: The authors express their gratitude to the Princess Nourah bint Abdulrahman University Researchers, Supporting Project Number (PNURSP2023R2), Princess Nourah bint Abdulrahman University, Riyadh, Saudi Arabia.

Institutional Review Board Statement: Not applicable.

Informed Consent Statement: Informed consent has been obtained from all individuals included in this study.

Data Availability Statement: The datasets generated during and/or analysed during the current study are available from the corresponding author on reasonable request.

Acknowledgments: Acknowledgments: The authors express their gratitude to the Princess Nourah bint Abdulrahman University Researchers, Supporting Project Number (PNURSP2023R2), Princess Nourah bint Abdulrahman University, Riyadh, Saudi Arabia.

Conflicts of Interest: Authors state no conflict of interest.

References

1. Lanfredi, S.; Gênova, D.H.; Brito, I.A.; Lima, A.R.; Nobre, M.A. Structural characterization and Curie temperature determination of a sodium strontium niobate ferroelectric nanostructured powder. *J. Solid-State Chem.* **2011**, *184*, 990–1000. [[CrossRef](#)]
2. Li, L.; Yang, B.; Chao, X.; Wu, D.; Wei, L.; Yang, Z. Effects of preparation method on the microstructure and electrical properties of tungsten bronze structure $\text{Sr}_2\text{NaNb}_5\text{O}_{15}$ ceramics. *Ceram. Int.* **2019**, *45*, 558–565. [[CrossRef](#)]
3. Josse, M.; Bidault, O.; Roulland, F.; Castel, E.; Simon, A.; Michau, D.; Von der Mühl, R.; Nguyen, O.; Maglione, M. The $\text{Ba}_2\text{LnFeNb}_4\text{O}_{15}$ “tetragonal tungsten bronze”: Towards RT composite multiferroics. *Solid State Sci.* **2009**, *11*, 1118–1123. [[CrossRef](#)]
4. Belarbi, M.; Tamraoui, Y.; Manoun, B.; Cantaluppi, A.; Gagou, Y.; Taibi, K.; El Marssi, M.; Lahmar, A. Structural, dielectric and energy storage properties of Neodymium niobate with tetragonal tungsten bronze structure. *Phys. B Condens. Matter* **2021**, *618*, 413185. [[CrossRef](#)]
5. Lanfredi, S.; Praxedes, F.R.; Ivashita, F.F.; Paesano, A., Jr.; Nobre, M.A.L. Suppression of ferroelectric phase-transition in niobates via solid solution formation. *Mater. Lett.* **2019**, *254*, 85–88. [[CrossRef](#)]
6. Botella, P.; Solsona, B.; Garcia-Gonzalez, E.; Gonzalez-Calbet, J.M.; Lopez Nieto, J.M. The hydrothermal synthesis of tetragonal tungsten bronze-based catalysts for the selective oxidation of hydrocarbons. *Chem. Comm.* **2007**, *47*, 5040–5042. [[CrossRef](#)]
7. Yang, B.; Hao, S.; Yang, P.; Wei, L.; Yang, Z. Relaxor behavior and energy storage density induced by B-sites substitutions in $(\text{Ca}_{0.28}\text{Ba}_{0.72})_2\text{.1Na}_{0.8}\text{Nb}_5\text{O}_{15}$ Tungsten bronze ceramics. *Ceram. Int.* **2018**, *44*, 8832–8841. [[CrossRef](#)]

8. Shimizu, K.; Kato, H.; Kobayashi, M.; Kakihana, M. Synthesis and photocatalytic properties of tetragonal tungsten bronze type oxynitrides. *Appl. Catal. B Environm.* **2017**, *206*, 444–448. [CrossRef]
9. Jindal, S.; Vasishth, A.; Devi, S.; Anand, G. A review on tungsten bronze ferroelectric ceramics as electrically tunable devices. *Integr. Ferroelectr.* **2018**, *186*, 1–9. [CrossRef]
10. Thummavichai, K.; Xia, Y.; Zhu, Y. Recent progress in chromogenic research of tungsten oxides towards energy-related applications. *Progress Mater. Sci.* **2017**, *88*, 281–324. [CrossRef]
11. Abrahams, S.C.; Jamieson, P.B.; Bernstein, J.L. Ferroelectric Tungsten Bronze-Type Crystal Structures. III. Potassium Lithium Niobate $K_{(6-x-y)}Li_{(4+x)}Nb_{(10+y)}O_{30}$. *J. Chem. Phys.* **1971**, *54*, 2355–2363. [CrossRef]
12. Lanfredi, S.; Brito, I.A.O.; Polini, C.; Nobre, M.A.L. Deriving the magnitude of niobium off-center displacement in ferroelectric niobates from infrared spectroscopy. *J. Appl. Spectrosc.* **2012**, *79*, 254–260. [CrossRef]
13. El, H.; Belghiti, A.; Simon, A.; Gravereau, P.; Villesuzanne, A.; Elaamrani, M.; Ravez, J. Ferroelectric and crystallographic properties of the $Sr_{2-x}K_{1+x}Nb_5O_{15-x}F_x$ solid solution. *Sol. State Sci.* **2002**, *4*, 933–940.
14. Reau, J.M.; Elouadi, B.; Ravez, J.; Hagemuller, P. Influence de la substitution tungstene-niobium sur les propriétés cristallographiques et diélectriques de la solution solide de compositions limites $Ba_{2.50-x}Na_{2x}Nb_5O_{15}$ ($0, 23 \leq x \leq 0, 60$). Le système $BaNb_2O_6(NaNbO_3)_2(WO_3)_2$ à $1050^\circ C$. *J. Solid State Chem.* **1975**, *15*, 18–23. [CrossRef]
15. Neqali, A.; Belboukhari, A.; Bensaid, H.; El Bouari, A.; Bih, L.; Alimoussa, A.; Habouti, S.; Mezzane, D. Diffuse phase transition and impedance spectroscopy analysis of $Ba_{2.15-x}Na_{0.7+x}Nb_{5-x}W_xO_{15}$ ($x = 0.25$) ferroelectric ceramic. *Appl. Phys. A* **2016**, *122*, 1–8. [CrossRef]
16. Chen, X.M.; Yang, J.S. Dielectric characteristics of ceramics in $BaO-Nd_2O_3-TiO_2-Ta_2O_5$ system. *J. Eur. Ceram. Soc.* **1999**, *19*, 139–142. [CrossRef]
17. Chen, X.M.; Liu, C.L.; Yang, J.S.; Wu, Y.J. Some Tungsten–Bronze Compounds in the $BaO-Nd_2O_3-TiO_2-Ta_2O_5$ System. *J. Solid State Chem.* **1999**, *148*, 438–441. [CrossRef]
18. Irvine, P.R.; Irvine, J.T.S. Synthesis and electrical characterisation of the tetragonal tungsten bronze type phases, $(Ba/Sr/Ca/La)_{0.6}M_xNb_{1-x}O_{3-\delta}$ ($M = Mg, Ni, Mn, Cr, Fe, In, Sn$): Evaluation as potential anode materials for solid oxide fuel cells. *Solid State Ion.* **1999**, *124*, 61–72.
19. Simon, A.; Ravez, J. Solid-state chemistry and non-linear properties of tetragonal tungsten bronzes materials. *C.R. Chim.* **2006**, *9*, 1268–1276. [CrossRef]
20. Stennett, M.C.; Miles, G.C.; Sharman, J.; Reaney, I.M.; West, A.R. A new family of ferroelectric tetragonal tungsten bronze phases, $Ba_2MTi_2X_3O_{15}$. *J. Eur. Ceram. Soc.* **2005**, *25*, 2471–2475. [CrossRef]
21. Stennett, M.C.; Reaney, I.M.; Miles, G.C.; Woodward, D.I.; West, A.R.; Kirk, C.A.; Levin, I. Dielectric and structural studies of $Ba_2MTi_2Nb_3O_{15}$ ($BMTNO_{15}$, $M = Bi^{3+}, La^{3+}, Nd^{3+}, Sm^{3+}, Gd^{3+}$) tetragonal tungsten bronze-structured ceramics. *J. Appl. Phys.* **2007**, *101*, 4114. [CrossRef]
22. Arnold, D.C.; Morrison, F.D. B-cation effects in relaxor and ferroelectric tetragonal tungsten bronzes. *J. Mater. Chem.* **2009**, *19*, 6485–6488. [CrossRef]
23. Zu, X.; Fu, M.; Stennett, M.C.; Villarinho, P.M.; Levin, I.; Randall, C.A.; Gardner, J.; Morrison, F.D.; Reaney, I.M. A crystal-chemical framework for relaxor versus normal ferroelectric behavior in tetragonal tungsten bronzes. *Chem. Matter* **2015**, *27*, 3250–3261.
24. Hu, C.; Fang, L.; Peng, X.; Li, C.; Wu, B.; Liu, L. Dielectric and ferroelectric properties of tungsten bronze ferroelectrics in $SrO-Pr_2O_3-TiO_2-Nb_2O_5$ system. *Mater. Chem. Phys.* **2010**, *121*, 114–117. [CrossRef]
25. Miller, A.J.; Rotaru, A.; Arnold, D.C.; Morrison, F.D. Effect of local A-strain on dipole stability in $A_6GaNb_9O_{30}$ ($A = Ba, Sr, Ca$) tetragonal tungsten bronze relaxor dielectrics. *Dalton Trans.* **2015**, *44*, 10738–10745. [CrossRef]
26. Available online: <https://materials.springer.com/bp/docs/978-3-540-31353-3> (accessed on 1 January 2005).
27. González-Abreu, Y.; Peláiz-Barranco, A.; Suarez-Gonzalez, L.C.; Guerra, J.D.S. Effects of polarons and oxygen vacancies on dielectric relaxation and electrical conductivity behavior in a lead-free relaxor ferroelectric. *J. Alloys Compd.* **2019**, *787*, 140–144. [CrossRef]
28. Rotaru, A.; Arnold, D.C.; Daoud-Aladine, A.; Morrison, F.D. Origin and stability of the dipolar response in a family of tetragonal tungsten bronze relaxors. *Phys. Rev. B* **2011**, *83*, 184302. [CrossRef]
29. Damjanovic, D. Ferroelectric, dielectric and piezoelectric properties of ferroelectric thin films and ceramics. *Rep. Prog. Phys.* **1998**, *61*, 1267. [CrossRef]
30. Rotaru, A.; Schiemer, J.A.; Carpenter, M.A. Elastic and anelastic relaxations accompanying relaxor dielectric behaviour of $Ba_6GaNb_9O_{30}$ tetragonal tungsten bronze from resonant ultrasound spectroscopy. *J. Therm. Anal. Calorim.* **2016**, *124*, 571–583. [CrossRef]
31. Chchiyai, Z.; El Bachraoui, F.; Tamraoui, Y.; Bih, L.; Lahmar, A.; Alami, J.; Manoun, B. Design, structural evolution, optical, electrical and dielectric properties of perovskite ceramics $Ba_{1-x}Bi_xTi_{1-x}Fe_xO_3$ ($0 \leq x \leq 0.8$). *Mater. Chem. Phys.* **2021**, *273*, 125096. [CrossRef]

32. Das, B.C.; Hossain, A.A. Rietveld refined structure, ferroelectric, magnetic and magnetoelectric response of Gd-substituted Ni-Cu-Zn ferrite and Ca, Zr co-doped BaTiO₃ multiferroic composites. *J. Alloys Compd.* **2021**, *867*, 159068. [CrossRef]
33. Sanjuán, M.L.; Kuhn, A.; Azcondo, M.T.; García-Alvarado, F. Proton and Deuteron Exchange in TTB-Like Na_{1.2}Nb_{1.2}W_{0.8}O₆: Structural Characterization and Spectroscopic Study. *Eur. J. Inorg. Chem.* **2008**, *2008*, 49–58. [CrossRef]
34. Ikeda, T.; Haraguchi, T.; Onodera, Y.; Saito, T. Some compounds of tungsten-bronze type A₆B₁₀O₃₀ (B = Nb, Ti or Nb, W). *Jpn. J. Appl. Phys.* **1971**, *10*, 987–994. [CrossRef]
35. Adachi, M.; Akishige, Y.; Asahi, T.; Deguchi, K.; Gesi, K.; Hasebe, K.; Hikita, T.; Ikeda, T.; Iwata, Y.; Komukae, M.; et al. “Ba₃Na₃MoNb₉O₃₀” in “Ferroelectric and Related Substances” Landolt-Börnstein—Group III Condensed Matter 36A2. Available online: <https://materials.springer.com/bp/docs/978-3-540-31349-6> (accessed on 3 February 2023).
36. Marinder, B.-O. Phases in the NaNbO₃-Nb₂O₅-WO₃ System: Derivation of Complex Structures by Twinning, Furling and Anti-phase-Boundary Operations on the ReO₃. Ph.D. Thesis, Stockholm University, Stockholm, Sweden, 1986.
37. Sundberg, M.; Marinder, B.-O. High resolution electron microscopy study in the NaNbO₃- Nb₂O₅- WO₃ system. *J. Solid State Chem.* **1990**, *84*, 23–38. [CrossRef]
38. Bouillaud, Y.; Bonnin, F. Stoechiométrie du métaniobate de sodium. *Bull. Soc. Fr. Miner. Crist.* **1965**, *88*, 700–701. [CrossRef]
39. Blasse, G.; dePauw, A.D.M. Crystal structure of some Li Me⁵⁺ Me⁶⁺ O₆ compounds. *J. Inorg. Nucl. Chem.* **1970**, *32*, 3960–3961. [CrossRef]
40. Thakre, O.B.; Chincholkar, V.S. New Compounds Of The A + B⁵⁺ B⁶⁺ O₆²⁻ Type I Structure. *Curr. Sci.* **1972**, *41*, 735–736.
41. Michel, C.; Groult, D.; Deschanvres, A.; Raveau, B. Propriétés d'échange d'ions des pyrochlores AB₂O₆—II Evolution thermique des pyrochlores AMWO₆. H₂O (A = Li, Na, Ag; M = Nb, Ta, Sb). *J. Inorg. Nucl. Chem.* **1975**, *37*, 251–255. [CrossRef]
42. Kuhn, A.; Bashir, H.; Dos Santos, A.L.; Acosta, J.L.; GarciaAlvarado, F. New protonic solid electrolyte with tetragonal tungsten bronze structure obtained through ionic exchange. *J. Solid State Chem.* **2004**, *177*, 2366–2372. [CrossRef]
43. Kuhn, A.; Azcondo, M.T.; Amador, U.; Boulahya, K.; Sobrados, I.; Sanz, J.; García-Alvarado, F. Structural Characterization and NMR Study of NaNbWO₆ and Its Proton-Exchanged Derivatives. *Inorg. Chem.* **2007**, *46*, 5390–5397. [CrossRef] [PubMed]
44. Es-soufi, H.; Bih, H.; Bih, L.; Rajesh, R.; Lima, A.R.F.; Sayyed, M.I.; Mezher, R. Rietveld Refinement, Structural Characterization, and Methylene Blue Adsorption of the New Compound Ba_{0.54}Na_{0.46}Nb_{1.29}W_{0.37}O₅. *Crystals* **2022**, *12*, 1695. [CrossRef]
45. Toby, B.H.; Von Dreele, R.B. GSAS-II: The genesis of a modern open-source all purpose crystallography software package. *J. Appl. Crystallogr.* **2013**, *46*, 544–549. [CrossRef]
46. Vaitkus, A.; Merkys, A.; Gražulis, S. Validation of the Crystallography Open Database using the Crystallographic Information Framework. *J. Appl. Crystallogr.* **2021**, *54*, 661–672. [CrossRef] [PubMed]
47. Sebastian, M.T. *Dielectric Materials for Wireless Communication*, 1st ed.; Elsevier Science: Amsterdam, The Netherlands, 2008.
48. Yanalak, G.; Ozen, A.; Sarilmaz, A.; Keles, A.; Aslan, E.; Ozel, F.; Patir, I.H. Scheelite-type BaMoO₄ and BaWO₄ based dye sensitized photocatalytic hydrogen evolution by water splitting. *J. Phys. Chem. Solids* **2022**, *168*, 110821. [CrossRef]
49. Nobrega, F.A.C.; Abreu, R.F.; Colares, D.D.M.; Silva, M.A.S.; do Carmo, F.F.; Abreu, T.O.; do Nascimento, J.P.C.; Sales, J.C.; Silva, R.S.; Goes, J.C.; et al. Influence of the addition of CaTiO₃ on the microwave dielectric properties of the BaMoO₄ matrix. *Mater. Chem. Phys.* **2022**, *289*, 126478. [CrossRef]
50. Shannon, R.D. Revised effective ionic radii and systematic studies of interatomic distances in halides and chalcogenides. *Acta Crystallogr. Sect. A Cryst. Phys. Diffr. Theor. Crystallogr.* **1976**, *32*, 751–767. [CrossRef]
51. Xu, S.; Peng, Z.; Shi, H.; Chao, X.; Wu, D.; Liang, P.; Yang, Z. Electrical conduction behavior in nonstoichiometric BaBixNb₅O_{15±δ} tungsten bronze ceramics. *Ceram. Int.* **2021**, *47*, 22382–22389. [CrossRef]
52. Wilde, R.E. Raman spectrum of Sr_{0.61}Ba_{0.39}Nb₂O₆. *J. Raman Spectrosc.* **1991**, *22*, 321. [CrossRef]
53. Liu, G.; Zhang, S.; Jiang, W.; Cao, W. Losses in ferroelectric materials. *Mater. Sci. Eng. R Rep.* **2015**, *89*, 1–48. [CrossRef]
54. Jebli, M.; Rayssi, C.; Dhahri, J.; Henda, M.B.; Belmabrouk, H.; Bajahzar, A. Structural and morphological studies, and temperature/frequency dependence of electrical conductivity of Ba_{0.97}La_{0.02}Ti_{1-x}Nb_{4x/5}O₃ perovskite ceramics. *RSC Adv.* **2021**, *11*, 23664–23678. [CrossRef]
55. Krupska-Klimczak, M.; Jankowska-Sumara, I.; Gwizd, P.; Koralewski, M.; Soszyński, A. Composition-Related Dielectric, Ferroelectric and Electrocaloric Properties of Pb₅Ge₃O₁₁ Single Crystals Modified by Ba Ions. *Materials* **2023**, *16*, 413. [CrossRef] [PubMed]
56. Lines, M.E.; Glass, A.M. *Principles and Applications of Ferroelectrics and Related Materials*; Oxford University Press Inc.: New York, NY, USA, 1977.
57. Dolgos, M.; Adem, U.; Wan, X.; Xu, Z.; Bell, A.J.; Comyn, T.P.; Stevenson, T.; Bennett, J.; Claridge, J.B.; Rosseinsky, M.J. Chemical control of octahedral tilting and off-axis A cation displacement allows ferroelectric switching in a bismuth-based perovskite. *Chem. Sci.* **2012**, *3*, 1426–1435. [CrossRef]
58. Godara, S.; Kumar, B. Effect of Ba–Nb co-doping on the structural, dielectric, magnetic and ferroelectric properties of BiFeO₃ nanoparticles. *Ceram. Int.* **2015**, *41*, 6912–6919. [CrossRef]

59. Connolly, T.F.; Hawkins, D.T. Tungsten Bronze Type and Layer Structure Oxides. *Ferroelectr. Lit. Index* **1974**, 161–174. [[CrossRef](#)]
60. Neurgaonkar, R.R.; Oliver, J.R.; Cross, L.E. Ferroelectric properties of tetragonal tungsten bronze single crystals. *Ferroelectrics* **1984**, *56*, 1035. [[CrossRef](#)]
61. Gagou, Y.; Dellis, J.L.; El Marssi, M.; Lukyanchuk, I.; Mezzane, D.; Elaammani, M. Ferroelectric Phases in Rare-Earth TTB Ferroelectric Compounds $Pb_{2(1-x)}K_{(1+x)}Gd_xNb_5O_{15}$. *Ferroelectrics* **2007**, *359*, 94–98. [[CrossRef](#)]
62. Taifi, E.; Lukyanchuk, I.; El Amraoui, Y.; Mezzane, D.; Gagou, Y. Monte Carlo study of ferroelectric properties of tetragonal tungsten bronze compounds. *Ferroelectrics* **2010**, *397*, 1–8. [[CrossRef](#)]
63. Duan, R.G.; Kuntz, J.D.; Garay, J.E.; Mukherjee, A.K. Metal-like electrical conductivity in ceramic nano-composite. *Scr. Mater.* **2004**, *50*, 1309–1313. [[CrossRef](#)]
64. Khaliullina, A.; Meshcherskikh, A.; Pankratov, A.; Dunyushkina, L. Effect of Sr Deficiency on Electrical Conductivity of Yb-Doped Strontium Zirconate. *Materials* **2022**, *15*, 4126. [[CrossRef](#)]
65. Hossen, M.B.; Alam, M.S.; Eman, N.M.; Shirin, N.J. Thermal response of dielectric, impedance and modulus spectroscopy study of NCZA bulk ceramics. *Phase Transit.* **2019**, *92*, 719–729. [[CrossRef](#)]

Disclaimer/Publisher's Note: The statements, opinions and data contained in all publications are solely those of the individual author(s) and contributor(s) and not of MDPI and/or the editor(s). MDPI and/or the editor(s) disclaim responsibility for any injury to people or property resulting from any ideas, methods, instructions or products referred to in the content.